geologica acta

Citation: Ali, S., Azer, K.M., Abdel-Karim, M.A., 2023. Origin and evolution of Neoproterozoic metaophiolitic mantle rocks from the Eastern Desert of Egypt: Implications for tectonic and metamorphic events in the Arabian-Nubian Shield. Geologica Acta, 21.6, 1-21, I-VII.

Online ISSN: 1696-5728 DOI: 10.1344/GeologicaActa2023.21.6

Origin and evolution of Neoproterozoic metaophiolitic mantle rocks from the Eastern Desert of Egypt: Implications for tectonic and metamorphic events in the Arabian-Nubian Shield

Shehata Ali[1] **Mokhles K. Azer**[2] **Abdel-Aal M. Abdel-Karim**[3]

[1]**Geology Department, Faculty of Science, Minia University**
P.O. 61519, El–Minia, Egypt. Tel.: + 201027029074. E-mail: shehata.ali@mu.edu.eg.

[2]**Geological Sciences Department, National Research Centre**
33 El Bohooth St. (former El Tahrir St.), Dokki, P.O. 12622, Giza, Egypt

[3] **Geology Department, Faculty of Science, Zagazig University**
P.O. 44519, Zagazig, Egypt

ABSTRACT

The mantle rocks from Kadaboura and Madara areas represent sections of dismembered ophiolitic complexes developed during the Neoproterozoic in the Eastern Desert of Egypt, which is located in the northwestern corner of the Arabian–Nubian Shield. The Kadaboura mantle rocks comprise serpentinites and serpentinized dunites, whereas those of the Madara consist of serpentinites and serpentinized pyroxenites.

Despite the serpentinization of the studied mantle rocks, few relicts of primary chromite, olivine and pyroxene are preserved. Chromite is partly altered having unaltered Al-rich chromite cores surrounded by Fe-rich chromite and Cr-rich magnetite rims. The unaltered Al-rich chromite cores show compositions equilibrated at temperatures mostly below ~500-600°C, which is a temperature comparable to that estimated for primary chromite in greenschist up to lower amphibolite facies rocks. The high Cr# [100×Cr/(Cr+Al)= 47-76] of the unaltered chromite cores and the Mg-rich nature of the olivine relicts ($Fo_{91–94}$) indicate that the studied mantle rocks were produced from a highly depleted mantle that experienced high degrees of melt extraction (mostly ~30-40%). This range of melt extraction resembles that estimated for supra-subduction zone peridotites, but higher than that in abyssal and passive margin peridotites. Furthermore, the clinopyroxene relicts show compositions comparable to those from the Mariana fore-arc peridotites. Bulk-rock geochemistry also reflects derivation from an extremely depleted and a highly refractory mantle source. Modeling of rare-earth elements suggests that the studied mantle rocks were possibly formed by the interaction of their highly depleted harzburgitic mantle precursors with subduction-related melts/fluids during their evolution in a fore-arc basin of the supra-subduction zone.

The proposed geodynamic model suggests that the oceanic lithosphere generated during the seafloor spreading of the Mozambique Ocean was emplaced in the upper plate of the intra-oceanic subduction zone, in which the formely depleted Neoproterozoic mantle of the Arabian-Nubian Shield experienced mature phases of hydrous melting, extreme depletion and enrichment.

KEYWORDS | **Mantle rocks. Ophiolite. Neoproterozoic serpentinite. Chromite. Eastern Desert. Egypt.**

INTRODUCTION

The Arabian-Nubian Shield (ANS) is a juvenile crust formed after the accretion of major fragments of East and West Gondwanaland during Neoproterozoic times (Abu-Alam *et al.*, 2013 and references therein). Ophiolite assemblages are significant elements of the ANS basement complexes since they delineate major suture zones and record tectonic and metamorphic events (*e.g.* Abdel-Karim *et al.*, 2018; Ali *et al.*, 2010; Stern *et al.*, 2003). The ANS ophiolites were formed at 690-890Ma and are common in Egypt, in the Central Eastern Desert (CED) and in the Southern Eastern Desert (SED) (Fig. 1A) (Abdel-Karim *et al.*, 2016, 2018; Ali *et al.*, 2021; Stern *et al.*, 2004). Formation of the ANS ophiolites and their tectonic emplacement may bring significant clues on the Gondwana supercontinent assembly during the Neoproterozoic (*e.g.* Stern *et al.*, 2004).

Ultramafic rocks in the Eastern Desert of Egypt (EDE) are rare and represent either parts of Alaskan-type (*e.g.* Abdallah *et al.*, 2019; Abdel-Rahman *et al.*, 2012; Helmy *et al.*, 2015) and layered intrusions (*e.g.* Abdel Halim *et al.*, 2016; Ahmed, 1991; Azer *et al.*, 2017; Dixon, 1981) or dismembered fragments of ophiolite assemblages (*e.g.* Abdel-Karim *et al.*, 2016, 2018; Ahmed *et al.*, 2012; Ali *et al.*, 2021). Alaskan-type intrusions comprise unaltered dunite-clinopyroxenite-gabbro associations usually hosting Cu-Ni-PGE deposits (*e.g.* Helmy, 2005), whereas layered-type intrusions consist of unaltered lherzolite, orthopyroxenite and gabbroic rocks (Abdel Halim *et al.*, 2016; Ali *et al.*, 2023; Azer *et al.*, 2017). The ophiolitic ultramafic rocks encompass intensely deformed serpentinites and scarce unaltered peridotites and pyroxenites (Abdel-Karim *et al.*, 2016, 2018; Azer and Stern, 2007; Farahat *et al.*, 2011). In the area, these rocks were subjected to greenschist and amphibolite facies metamorphism (*e.g.* Abdel-Karim *et al.*, 2018; Ali *et al.*, 2021; El-Sayed *et al.*, 1999; Khedr and Arai, 2013).

The tectonic emplacement of the ANS ophiolite complexes is under debate (Abdel-Karim *et al.*, 2016; Ali *et al.*, 2021; El Bahariya, 2018; Farahat *et al.*, 2011; Khedr and Arai, 2013; Zimmer *et al.*, 1995). However,

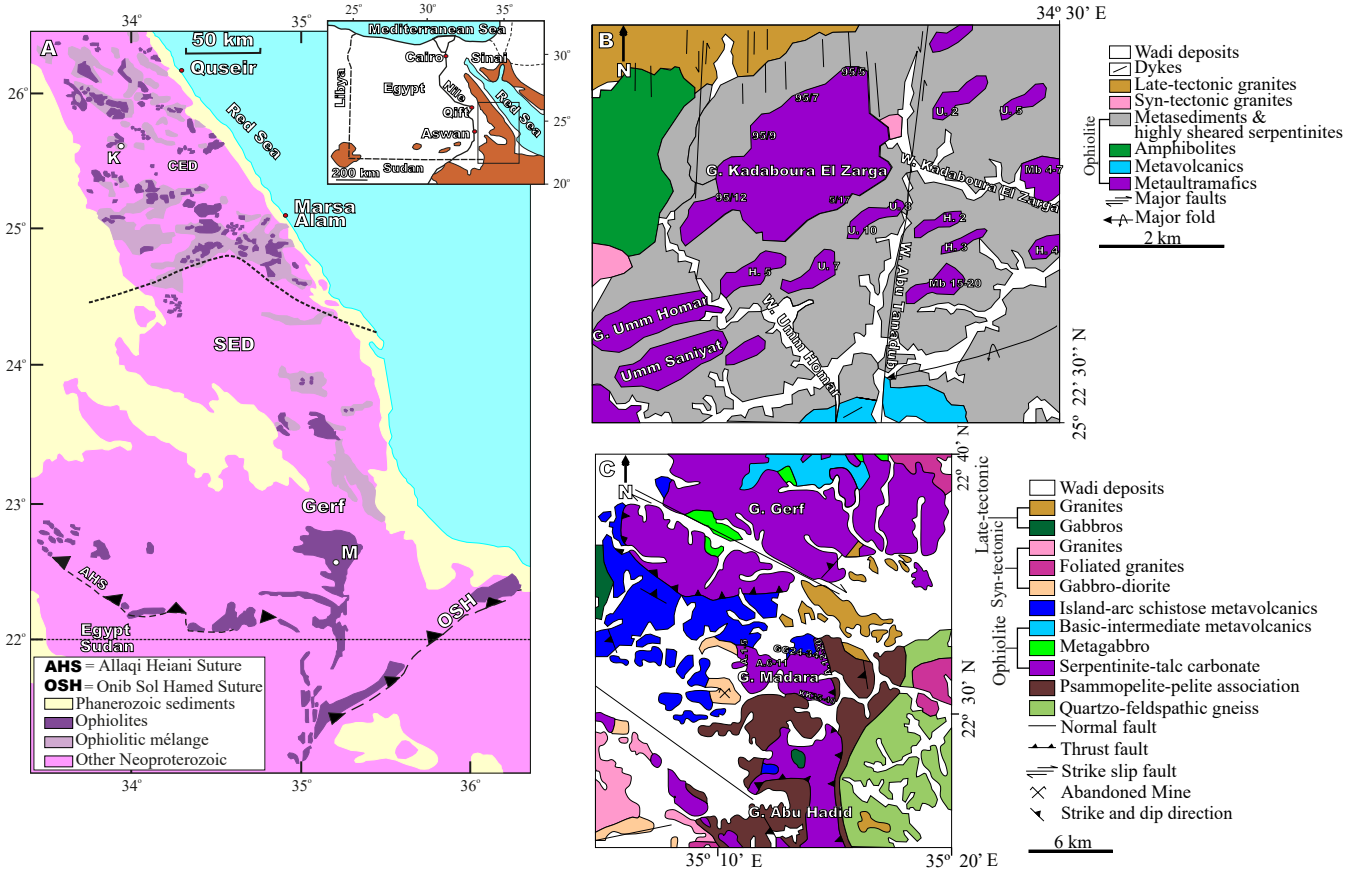

FIGURE 1. A) Distribution of ophiolites in the Eastern Desert of Egypt (EDE) and location of Kadaboura (K) and Madara (M) ophiolites (after Shackleton, 1994). SED = Southern Eastern Desert; CED = Central Eastern Desert. Inset: general map of Egypt showing location of Figure 1A. Brown color in the inset refers to basement rocks. B) Geologic map of Kadaboura in the Central Eastern Desert (CED; after Abdel-Karim *et al.*, 1997). C) Geologic map of Madara in the Southern Eastern Desert (SED; after Hassan and Sadek, 2017).

a Supra-Subduction Zone (SSZ) setting is widely accepted for these ophiolites (*e.g.* Abdel-Karim *et al.*, 2016, 2018; Ahmed *et al.*, 2012; Ali *et al.*, 2021; Azer and Stern, 2007; Farahat *et al.*, 2011; Stern *et al.*, 2004). Data from mineral chemistry and lava composition suggest that most of the ANS ophiolites were formed in SSZ settings, and the high Cr# [100×Cr/(Cr+Al)] values of the chromites in the ANS ophiolitic harzburgites reveal development in a fore-arc basin (Gahlan *et al.*, 2015; Stern *et al.*, 2004). Also, the ophiolitic ultramafic segments in the EDE show mineral and bulk-rock geochemistry consistent with a fore-arc setting (Abdel-Karim *et al.*, 2016, 2018; Ali *et al.*, 2021; Azer and Stern, 2007; Azer *et al.*, 2013).

Ophiolite complexes in the CED of Egypt exhibit both MORB (Mid-Ocean Ridge Basalt)- and SSZ-type affinities (El Bahariya, 2018). According to geologic features and occurrences, El Bahariya (2018) classified them from oldest to youngest into MORB intact ophiolites, MORB- and SSZ-type dismembered ophiolites, and SSZ-related intact ophiolites. The dismembered ophiolites are found as blocks in mélanges or along structural contacts (El Bahariya, 2018). Ophiolite complexes in the SED of Egypt occur along the Allaqi-Heiani and Onib-Sol Hamed major suture zone (Fig. 1A). Their mantle sections show affinity to the SSZ-type (fore-arc) ophiolites (*e.g.* Abdel-Karim *et al.*, 2016, 2018; Khalil *et al.*, 2014; Sedki *et al.*, 2019).

This study presents new field and petrographic features as well as mineral and bulk-rock data of metamorphosed mantle rocks from Kadaboura El-Zarga (hereafter Kadaboura) and Madara areas in the EDE (Fig. 1) to better constrain their geochemical evolution as well as to shed light into the tectonic and metamorphic events that prevailed during the Neoproterozoic.

GEOLOGICAL SETTING

Pan-African nappes in the ANS comprise low-grade metamorphosed ophiolites together with arc-related metavolcanic and metasedimentary rocks (Stern *et al.*, 2004). Ophiolite assemblages are scattered over ~3000km across most of the ANS and cover an area of ~2 million km^2. They are common in the EDE (Fig. 1A) and encompass pillow metabasalts, metagabbros and metamorphosed ultramafic rocks (Abu El-Ela, 1996; El-Sharkawy and El-Bayoumi, 1979). The metamorphosed ultramafic rocks are partially or completely serpentinized. They comprise mostly serpentinites and serpentinized peridotites, occasionally with chromitite pods, listwaenites, talc-carbonate rocks and magnesite veins.

Kadaboura

Kadaboura mantle rocks (Fig. 1B) are part of the W. Mubarak ophiolitic mélange. This mélange is formed of allochthonous, dismembered, variably sized blocks and sheets in a matrix of deformed metasedimentary rocks, and highly sheared serpentinites. The mélange blocks include metamorphosed ultramafics, metagabbros, metavolcanics and amphibolites. The metamorphosed ultramafics are the most common among the mélange blocks, being represented almost entirely by serpentinites and talc-carbonate rocks (Fig. 2A). The serpentinites occur as elongated thrust sheets trending NE-SW and embedded in and resting over metasedimentary mélange matrix (*e.g.* Kadaboura, Umm Homar and Umm Saniyat, and around W. Kadaboura, W. Abu Tanadub). Serpentinized dunites occur as small lenses. The ophiolitic mélange was intruded by syn- to late-tectonic granites and is crosscut by dikes of variable compositions. All these rocks are dissected by two major N-S extending left-lateral strike-slip faults, running throughout W. Abu Tanadoub and W. Kab El-Rakeb El-Ghabubi. Both faults extend further north of the study area for ~40km. The axial traces of the three major overturned folds encountered in the area are

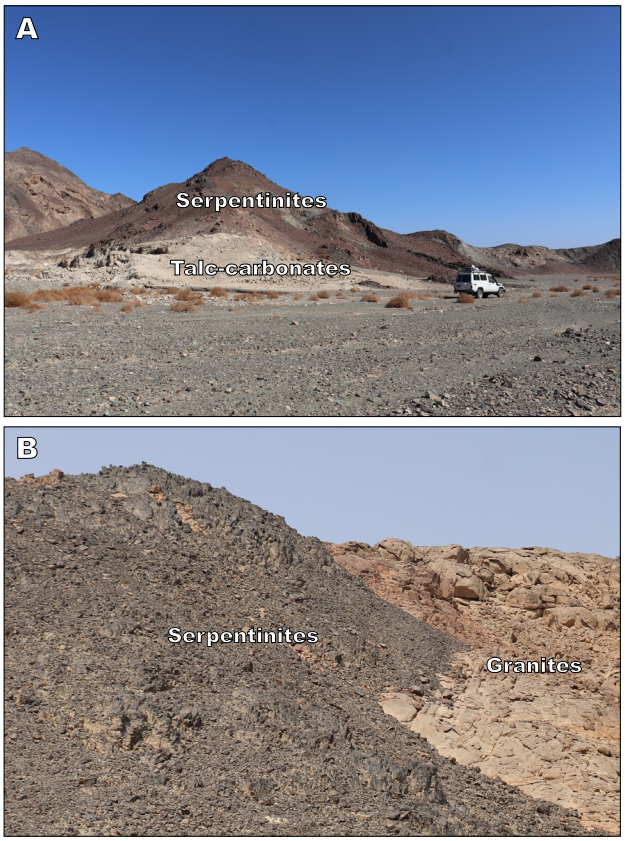

FIGURE 2. Field photographs showing A) Serpentinites and talc-carbonates in Kadaboura area; B) Granite-intruded serpentinites in Madara area.

shifted in a sinistral-slip manner along the planes of these faults.

Madara

Madara mantle rocks (Fig. 1C) occur as lenses and sheet-like bodies of massive serpentinites and pyroxenites within the W. Mubarak ophiolite mélange. The massive serpentinites are the most abundant rocks in the area and occur as high relief (1300m) hills. Pyroxenites are less abundant and occur as unmappable pockets, lenses or veins within the serpentinites. These rocks exist as masses of medium-grained rocks with a dark gray to black color. Folded bands of talc-carbonate rocks occur along shear zones between serpentinites and other ophiolitic units. White alteration spots of talc-carbonate rocks have been observed mainly close to thrust contacts. In the northern parts of the Gerf belt, the serpentinites were thrusted above the metagabbro and metavolcanic rocks. Serpentinites were intruded by syn- to late-tectonic granites with sharp contacts (Figs. 1C; 2B). The structural history of the ophiolite mélange includes three episodes of deformations (D1, D2 and D3; Abdel-Karim *et al.*, 2001). The D1 event generated major overturned folds having NW-SE trending axial traces with NW-plunged axes. Folds formed during D2 are open with N-S trending axial traces and NNW plunged axes. Those produced during D3 are extra open compared to the previously formed ones and have NNE-SSW trending axial traces with WNW plunged axes.

METHODOLOGY

Electron probe microanalyses of minerals were performed on polished thin sections of six representative samples from the studied areas (samples 95/5, 95/17, 19 and KD217 are from Kadaboura and samples A and KK37b are from Madara). Chemical analyses were performed on silicates (olivine, pyroxene, amphibole, serpentine, talc, chlorite) and non-silicates (chromite, carbonate). The analyses were performed with a JEOL JXA-8500F electron probe at the Washington State University (WSU). Operating conditions were 15kV accelerating voltage, 20nA beam current and 1μm focused beam. A mix of appropriate standards from natural and synthetic minerals was used for calibrations (Table I of the Appendix). Detection limits and precision of the analyses are given on the laboratory website (https://environment.wsu.edu/facilities/geoanalytical-lab). The analyses of various minerals are listed in Tables II-IX.

Eighteen representative rock samples were used for geochemical analyses. The rock samples were cleaned and grinded using an electric agate mill. The powdered samples were homogenized, dried on the oven for 60min at 110°C, and ignited at 950°C. Major oxides and trace elements were measured using a Philips PW 2400 series X-ray spectrometer on fused glass beads at the Earth Science Institute, Vienna University, Austria. The relative analytical precision is around 1% for major and 2% for trace elements. LOI (Loss On Ignition) was measured after ignition of 5g of sample powder in porcelain crucibles at 1050°C for 1h. Rare Earth Element (REE) analyses were measured at the Institute of Inorganic Chemistry, Vienna University, Austria by VG Elemental PQ3 Quadruple Inductively Coupled Plasma-Mass Spectrometer. Precision and accuracy were tested using international standards (including African Mineral standards; AMIS 0007) and by analyzing blanks and duplicates. The bulk-rock chemical analyses are given in Table 1.

PETROGRAPHY

The studied ophiolitic ultramafic rocks are partially or completely serpentinized. Kadaboura includes serpentinite and serpentinized dunite, whereas Madara comprises serpentinite and serpentinized pyroxenite.

The serpentinites of both areas comprise both massive and sheared varieties. In places, the serpentinites preserve minor relicts of olivine and clinopyroxene (Fig. 3A, B). They consist basically of serpentine minerals, together with minor contents of carbonates, talc, chromite, chlorite, tremolite and magnetite. The abundance of mesh and bastite textures in the studied serpentinites indicate alteration after olivine and orthopyroxene supporting harzburgite protolith. Chromite is partly altered and shows unaltered chromite cores surrounded by magnetite rims. Serpentine minerals are either antigorite or aggregates of antigorite, lizardite and chrysotile (Fig. 3 C, D). Antigorite occurs as fibrolamellar aggregates of anhedral to subhedral crystals that resulted from complete alteration of olivine. It is partially replaced by talc, carbonate and magnetite. Locally, fibrous antigorite crystals show fan-shaped bundles (Fig. 3C). Lizardite occurs as extremely fine-grained flakes and massive interstitial aggregates, whereas chrysotile occurs as minute fibrous aggregates and veins (Fig. 3D). Cross-fiber chrysotile veins alternate with antigorite/lizardite aggregates (Fig. 3D). Chlorite forms fine irregular flakes spread randomly through other mineral constituents. Talc occurs as fine-crystalline aggregates. Carbonate forms interstitial patches associated with disseminated grains of magnesite. The serpentinite textures include mesh and interpenetrating textures (Fig. 3E).

Serpentinized dunites in Kadaboura area consist of variable amounts of serpentine phases (*i.e.* antigorite, chrysotile veins) and olivine relicts (Fig. 3F) together with talc, chromite, and magnetite. Olivine relicts are common in serpentinized dunite compared to serpentinite and

TABLE 1. Bulk-rock major (wt.%), trace and rare-earth elements (ppm) geochemistry of the studied mantle rocks

Area	Kadaboura								Madara										Detection limit
Rock type	Dunites				Serpentinites				Serpentinites							Orthopyroxenites			
Sample No.	95/5	Mb4	Mb7	Mb15	U.7	H.4	95/17	Mb20	A3	A12	A15	A19	KK37b	KK38	KK40	A	GG24	GG34	
SiO_2	40.90	39.60	39.80	41.09	44.23	44.67	42.40	41.82	45.65	45.41	46.95	47.11	43.22	44.00	44.34	55.98	52.61	54.21	0.01 wt.%
TiO_2	0.10	0.10	0.10	0.12	0.21	0.13	0.14	0.17	0.14	0.15	0.15	0.17	0.07	0.03	0.09	0.06	0.09	0.06	0.01 wt.%
Al_2O_3	2.80	2.75	2.92	3.70	4.23	4.34	2.72	4.07	1.18	1.39	1.07	1.37	0.79	1.23	1.35	0.69	0.82	0.86	0.01 wt.%
Fe_2O_3 ^{total}	8.36	8.49	8.42	6.50	7.54	6.16	7.26	8.02	6.98	8.09	7.28	7.48	8.76	8.80	8.06	6.09	4.75	6.60	0.01 wt.%
MnO	0.06	0.06	0.07	0.06	0.06	0.09	0.04	0.07	0.14	0.10	0.18	0.09	0.14	0.09	0.09	0.13	0.16	0.20	0.01 wt.%
MgO	41.02	41.92	40.66	40.62	35.86	36.71	40.15	37.13	44.69	43.82	43.23	42.44	45.57	43.71	44.87	33.86	36.17	33.11	0.01 wt.%
CaO	4.87	4.77	5.00	6.10	5.81	4.03	3.78	5.17	0.26	0.15	0.39	0.48	0.86	0.80	0.74	2.76	3.50	2.94	0.01 wt.%
Na_2O	0.12	0.14	0.12	0.12	0.14	0.24	0.09	0.13	0.06	0.03	0.05	0.05	<0.01	0.01	<0.01	0.03	0.03	0.05	0.01 wt.%
K_2O	0.09	0.08	0.10	0.08	0.07	0.11	0.06	0.10	0.03	0.02	0.04	0.02	0.01	<0.01	<0.01	<0.01	<0.01	<0.01	0.01 wt.%
P_2O_5	1.26	1.19	1.26	0.10	1.19	2.71	2.41	1.47	0.05	0.06	0.12	0.07	0.54	0.38	0.25	0.17	0.22	0.29	0.01 wt.%
Total	99.58	99.10	98.45	98.49	99.35	99.18	99.05	98.15	99.17	99.23	99.45	99.27	99.96	99.07	99.80	99.77	98.35	98.32	
LOI	13.23	16.07	10.19	16.42	15.91	15.29	14.70	15.63	11.89	12.77	15.82	12.18	14.04	13.94	13.35	10.47	8.22	1.76	
Mg#	90.71	90.76	90.57	92.56	90.44	92.23	91.67	90.20	92.73	91.51	92.20	91.86	91.19	90.81	91.72	91.71	93.82	90.89	
Cr	865	908	812	1230	1150	1005	996	1066	3221	2345	2113	3425	3101	2529	2318	2030	62	58	1 ppm
Ni	969	1004	845	1321	1432	1244	1326	1462	2233	2456	1765	2342	2756	2563	2639	2080	65	77	1 ppm
Sc	6.00	5.00	7.00	4.00	4.30	2.00	7.00	3.20	10.30	11.00	15.00	28.00	7.30	8.10	8.30	1.00	1.00	1.00	1 ppm
Ba	20.60	18.00	15.00	17.20	20.50	26.80	32.80	15.60	2.00	3.00	5.00	4.00	4.20	5.60	3.40	8.00	6.10	6.50	1 ppm
Co	154.30	174.00	168.00	154.00	167.50	176.60	185.80	161.00	68.00	58.00	115.00	95.00	97.00	101.00	112.00	42.00	2.00	1.50	0.1 ppm
Ga	12.00	10.00	11.00	15.00	18.00	20.00	15.00	17.60	4.00	5.00	3.00	1.30	1.10	1.60	1.40	1.00	1.00	1.00	0.5 ppm
Hf	0.070	0.100	0.110	<0.10	0.080	0.140	0.130	0.120	0.060	0.090	0.200	0.070	0.100	0.100	0.100	0.300	0.500	0.500	0.01 ppm
Ta	0.070	0.100	0.120	0.120	0.150	0.090	0.110	0.100	0.140	0.120	0.100	0.120	0.100	0.100	0.100	0.100	0.210	0.300	0.01 ppm
Th	0.31	0.35	0.24	0.16	0.18	0.60	0.09	0.10	0.09	0.08	0.15	0.15	0.20	0.10	0.10	0.07	0.05	0.04	0.01 ppm
U	0.05	0.04	0.06	0.07	0.09	0.40	0.08	0.05	0.05	0.05	0.07	0.09	0.10	0.10	0.10	0.15	0.18	0.20	0.01 ppm
Nb	0.09	0.05	0.06	1.00	0.06	0.08	0.05	1.00	0.10	0.25	0.20	0.15	0.10	0.10	0.10	2.00	2.60	2.52	0.01 ppm
Rb	2.00	2.00	3.00	0.50	0.30	1.00	0.43	0.75	2.30	2.50	0.10	0.20	0.80	0.60	1.10	3.00	5.00	2.00	0.01 ppm
Sr	70.70	68.40	74.00	62.00	80.50	85.40	69.50	60.50	4.00	6.10	3.10	2.00	4.10	65.00	7.30	3.00	3.00	7.00	1 ppm
V	50.50	66.00	64.00	55.00	68.80	85.40	67.40	63.00	105.00	121.00	67.00	135.00	68.40	60.70	83.90	15.00	20.00	27.00	10 ppm
W	2.60	2.50	2.10	2.40	3.80	0.45	4.03	2.30	0.35	0.40	2.00	0.45	1.20	1.50	0.90	2.00	5.00	8.00	0.4 ppm
Zr	5.20	5.00	4.60	3.80	4.60	7.10	6.70	4.00	5.00	3.10	4.10	3.50	0.80	0.60	1.20	16.00	22.00	20.50	0.1 ppm
Y	2.30	2.30	2.80	2.00	2.00	2.50	1.50	1.60	4.00	4.20	3.00	3.00	0.70	0.60	0.50	6.00	8.00	7.60	0.1 ppm
Mo	0.17	0.12	0.20	1.00	<0.1	0.14	1.30	1.00	<0.1	<0.1	0.20	0.30	0.10	<0.1	0.20	2.00	3.00	7.00	0.1 ppm
Cu	31.20	27.30	30.50	36.10	45.20	34.20	29.60	35.40	24.43	21.70	6.33	14.32	7.80	11.70	5.90	4.00	7.00	2.00	0.1 ppm
Pb	1.80	1.20	1.00	10.00	12.40	10.30	8.90	8.00	9.00	6.00	13.23	1.45	3.60	2.60	1.50	5.00	12.00	7.00	0.1 ppm
Zn	54.00	44.00	52.00	54.00	65.00	88.60	72.20	53.00	43.00	56.00	19.40	15.00	16.50	11.20	22.10	56.00	84.00	84.00	1 ppm
Au	5.77	3.12	2.45	0.87	0.95	3.50	4.23	1.6	4.43	3.28	6.21	5.30	0.0122	0.0038	0.0016	3.20	3.40	2.77	0.5 ppb
La	0.100	0.090	0.150	0.110	0.120	0.190	0.140	0.130	0.360	0.130	0.150	0.350	0.330	0.250	0.240	2.000	1.680	2.420	0.1 ppm
Ce	0.140	0.120	0.190	0.060	0.070	0.050	0.100	0.700	0.460	0.090	0.190	0.450	0.750	0.580	0.490	3.100	2.760	3.510	0.01 ppm
Pr	0.010	0.008	0.016	0.033	0.040	0.060	0.050	0.052	0.230	0.040	0.050	0.210	0.090	0.080	0.060	0.550	0.430	0.460	0.01 ppm
Nd	0.090	0.080	0.120	0.200	0.230	0.320	0.270	0.260	0.700	0.060	0.080	0.670	0.390	0.310	0.280	2.450	2.380	2.780	0.03 ppm
Sm	0.010	0.008	0.012	0.020	0.030	0.080	0.060	0.040	0.410	0.060	0.090	0.390	0.110	0.090	0.070	0.640	0.540	0.700	0.01 ppm
Eu	0.010	0.007	0.017	0.020	0.020	0.090	0.050	0.030	0.100	0.030	0.050	0.090	0.020	0.030	0.010	0.380	0.340	0.420	0.01 ppm
Gd	0.020	0.016	0.024	0.020	0.030	0.050	0.050	0.040	0.300	0.070	0.090	0.280	0.130	0.110	0.080	0.910	0.860	0.120	0.01 ppm
Tb	0.010	0.008	0.013	0.020	0.030	0.070	0.050	0.040	0.100	0.050	0.060	0.070	0.010	0.010	0.010	0.160	0.140	0.190	0.01 ppm
Dy	0.060	0.050	0.080	0.062	0.070	0.020	0.050	0.084	0.290	0.020	0.040	0.270	0.170	0.130	0.090	1.110	1.000	1.430	0.01 ppm
Ho	0.050	0.040	0.060	0.032	0.040	0.010	0.030	0.046	0.100	0.040	0.040	0.090	0.040	0.020	0.020	0.180	0.150	0.210	0.01 ppm
Er	0.027	0.022	0.030	0.030	0.038	0.100	0.080	0.042	0.190	0.020	0.060	0.170	0.110	0.080	0.070	0.560	0.500	0.620	0.01 ppm
Tm	0.029	0.031	0.036	0.040	0.048	0.070	0.050	0.054	0.100	0.030	0.060	0.090	0.010	0.010	0.010	0.080	0.070	0.110	0.01 ppm
Yb	0.068	0.070	0.070	0.041	0.047	0.018	0.055	0.053	0.300	0.040	0.070	0.280	0.110	0.090	0.080	0.580	0.500	0.600	0.01 ppm
Lu	0.070	0.055	0.082	0.037	0.040	0.030	0.050	0.048	0.100	0.050	0.060	0.080	0.010	0.010	0.010	0.090	0.070	0.120	0.01 ppm

Mg#=100×Mg/(Mg+Fe^{2+})

serpentinized pyroxenite. On the other hand, pyroxene relicts are not observed in the serpentinized dunite. Serpentine phases after olivine display mesh texture (Fig. 3G). The olivine mesh center is formed due to serpentinization of olivine along grain boundaries and fractures. Few magnesite patches are also present (Fig. 3G). Chromite shows characteristic pull-apart textures (Fig. 3H) due to tensional force occurred during plastic deformation (Engin *et al.*, 1980).

Serpentinized pyroxenites in the Madara area consist mainly of orthopyroxene and serpentine associated with minor clinopyroxene and olivine relicts. Chromite and magnetite are the main accessory minerals. The rocks show allotriomorphic granular texture. Orthopyroxene forms pale green coarse prismatic crystals. In some samples, orthopyroxene is completely sheared and altered to tremolite-actinolite and chlorite. Clinopyroxene shows a pale pinkish color. Olivine forms scattered colorless fractured crystals partially or completely altered to serpentine. Bastite texture after orthopyroxene is also observed (Fig. 3I). Orthopyroxene and clinopyroxene crystals form porphyroblastic textures (Fig. 3J). Xenomorphic grains and irregular patches of chromite are also observed. Magnetite occurs as fine dusty aggregates concentrated around partially altered orthopyroxene crystals or as secondary coronas over chromite.

MINERAL CHEMISTRY

Chromite

Data of the analyzed chromite from serpentinites of both areas are listed in Table II. The unaltered cores show high Cr# (47–76) with Mg# [100×Mg/(Mg+Fe^{2+})] (21–68). Altered rims have higher Cr# (82–99) and lower Mg# (2–25) compared to unaltered cores. Based on the Cr# vs. Mg# diagram, the core compositions range from chromite to magnesiochromite, whereas the rims are

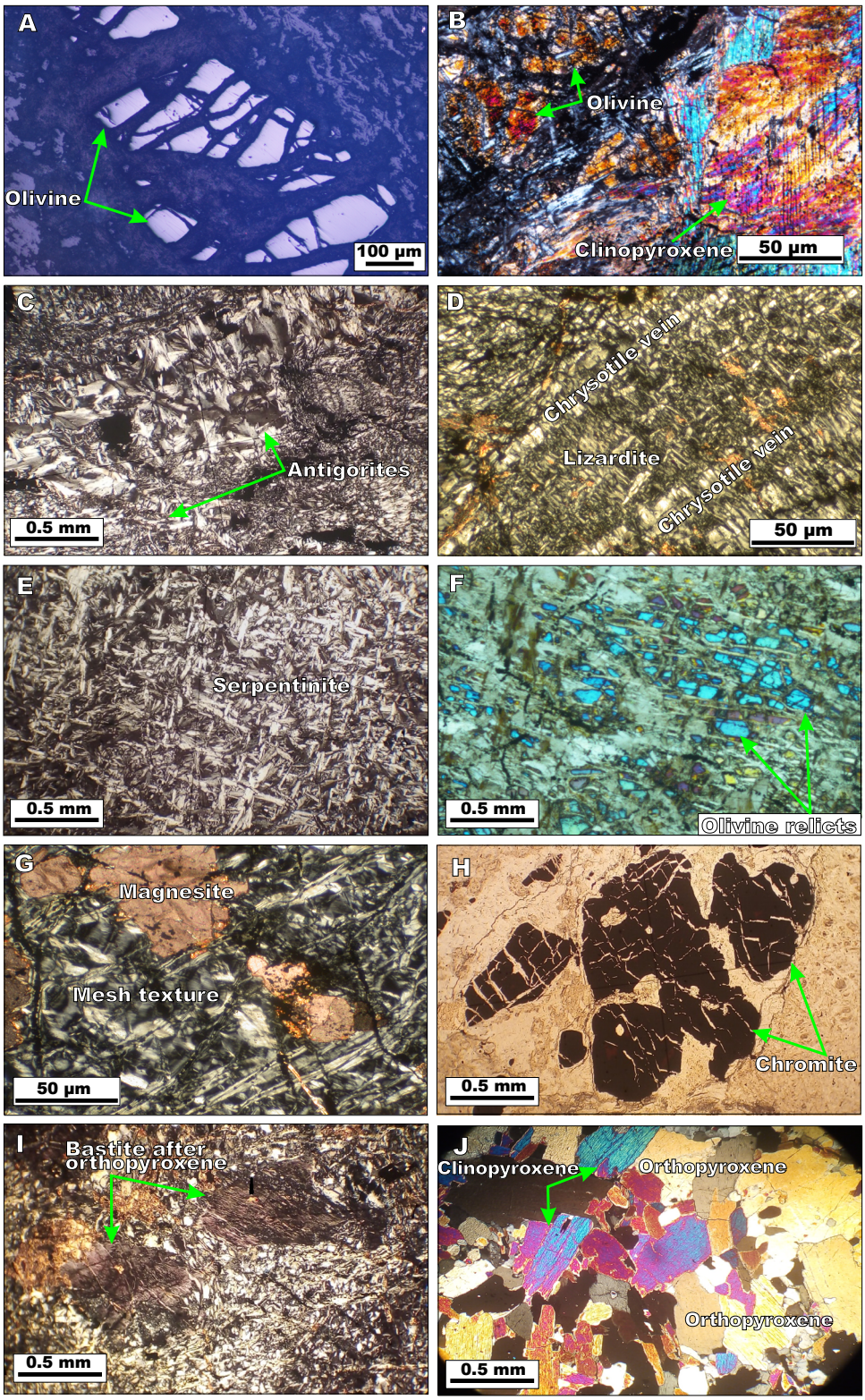

FIGURE 3. Photomicrographs showing the main petrographic features under crossed nicols except A (Back-Scattered Electron; BSE) and H (plain polarized light). A) Primary olivine altered along cracks in Kadaboura serpentinite (sample U.7). B) Fresh clinopyroxene with olivine relicts in Kadaboura serpentinite (sample H.4). C) Fan-shaped bundles of antigorite crystals within Madara serpentinite (sample A.12). D) Veins of cross-fiber chrysotile alternate with lizardite in Madara serpentinite (sample A.15). E) Interpenetrating texture in Madara serpentinite (sample A.15). F) Olivine relicts in Kadaboura serpentinized dunite (sample 95/5). G) Mesh texture and magnesite patch in Kadaboura serpentinized dunite (sample 95/5). H) Pull-apart texture in chromite within Kadaboura serpentinized dunite (sample Mb4). I) Bastite texture in Madara serpentinized orthopyroxenite (sample GG24). J) Porphyroblastic texture in Madara serpentinized orthopyroxenite (sample GG34).

chromite (Fig. 4A). In the Cr-Fe^{3+}-Al ternary relationship (Fig. 4B), the unaltered cores are classified as Al-rich chromite and are like unaltered chromite of greenschist and lower amphibolite facies. Altered rims are mainly Cr-rich magnetite with few Fe-rich chromite (Fig. 4B). The unaltered Al-rich chromite cores plot along the Cr-Al join, while the altered Fe-rich chromite and Cr-rich magnetite rims plot nearby the Cr-Fe^{3+} join (Fig. 4B). Moreover, the compositions of the unaltered cores are like those in arc peridotites of SSZ (*e.g.* New Caledonia and Mariana arcs; Fig. 4C, D). They have Cr# values higher than those of the abyssal peridotites but like those of the fore-arc peridotites (Fig. 4A). Their Cr, Fe^{3+} and Al contents are plotted within the fore-arc peridotites field (Fig. 4B). A tendency toward boninites is also observed (Fig. 4D).

Olivine

Olivine relicts show a compositional range ($Fo_{91–94}$; Table III) like that of primary olivine of mantle rocks in the Egyptian Eastern Desert ophiolites ($Fo_{89–96}$) (Abdel-Karim *et al.*, 2018; Khalil and Azer, 2007; Khedr and Arai, 2013; Moussa *et al.*, 2021, 2022; Obeid *et al.*, 2016). The high Fo contents are akin to those in the ANS ophiolitic ultramafic rocks and fore-arc peridotites (Abuamarah *et al.*, 2020; Stern *et al.*, 2004) but are clearly distinct from those in olivine from the non-ophiolitic mafic-ultramafic intrusions in the ANS (Fo= 77.5-86.5: Abd El-Rahman *et al.*, 2012; Azer and El-Gharbawy, 2011; Azer *et al.*, 2016, 2017; Farahat and Helmy, 2006; Gahlan *et al.*, 2023; Ghoneim, 1989; Helmy and El Mahallawi, 2003). Their Fo and NiO contents fall within the range of the SSZ ophiolitic serpentinites of the EDE and overlap those of the olivine mantle array (Fig. 5A).

Pyroxene

Pyroxene relicts comprise ortho- and clinopyroxene compositions (Table IV). Orthopyroxene compositions are enstatite ($En_{0.88–0.91}$) (Fig. 5B) with elevated Mg# (90–92). The Cr_2O_3 (0.45-0.80wt.%) and CaO (0.58-1.49wt.%) contents are higher than the rang of these oxides for the metamorphic orthopyroxene (mostly Cr_2O_3<0.60wt.%, and CaO<0.25wt.%), suggesting a primary nature (Nozaka,

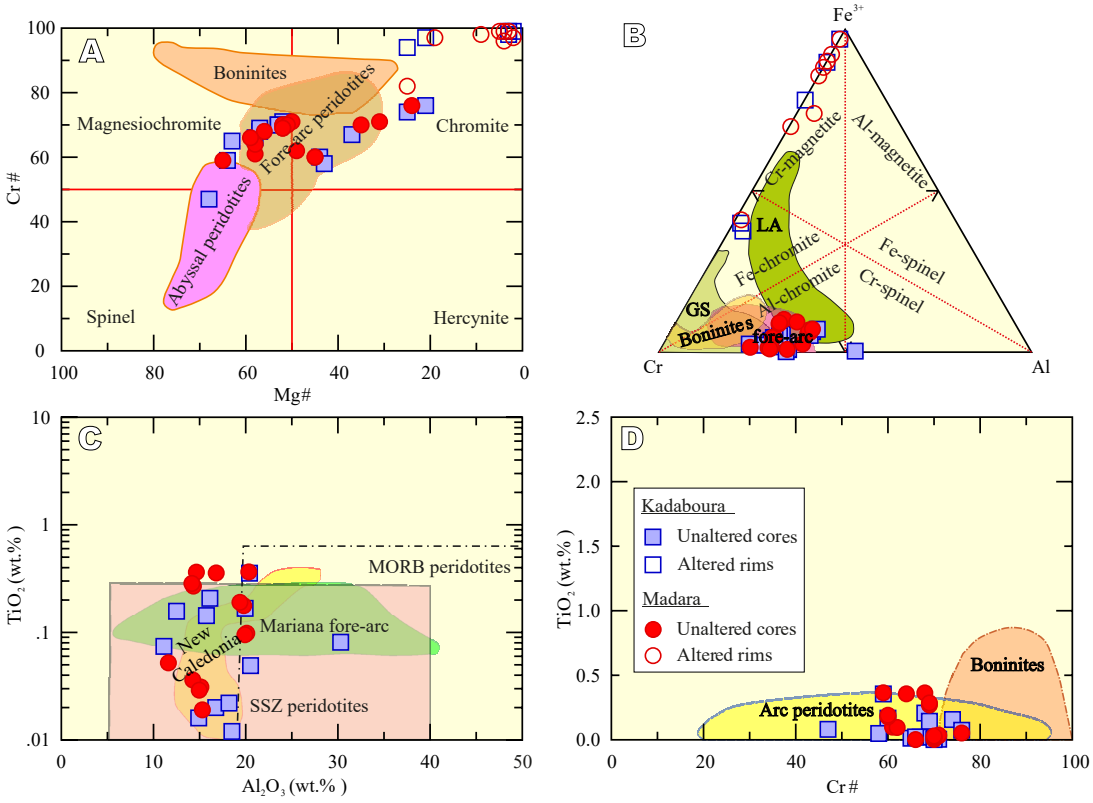

FIGURE 4. Plots of chromite compositions. A) Cr# vs. Mg# classification diagram (Kapsiotis *et al.*, 2009). Data sources: boninites (Barnes and Roeder, 2001; Kepezhinskas *et al.*, 1993); fore-arc (Parkinson and Pearce, 1998); abyssal peridotites (Dick and Bullen, 1984). B) Cr-Fe^{3+}-Al ternary classification diagram (Stevens, 1944). Data sources: Greenschist (*GS*) and lower-amphibolite (*LA*) metamorphic facies (Evans and Frost, 1975; Suita and Strieder, 1996); boninites (Barnes and Roeder, 2001 and references therein); fore-arc peridotites (Ishii *et al.*, 1992; Parkinson and Pearce, 1998). C) Al_2O_3-Ti_2O diagram. Fields correspond to accessory chromite in SSZ and MORB-type peridotites, as well as Mariana and New Caledonia fore-arc peridotites are after Kamenetsky *et al.* (2001). D) Cr# vs. TiO_2 diagram. Fields correspond to accessory chromite in boninites and arc peridotites are from Python *et al.* (2008).

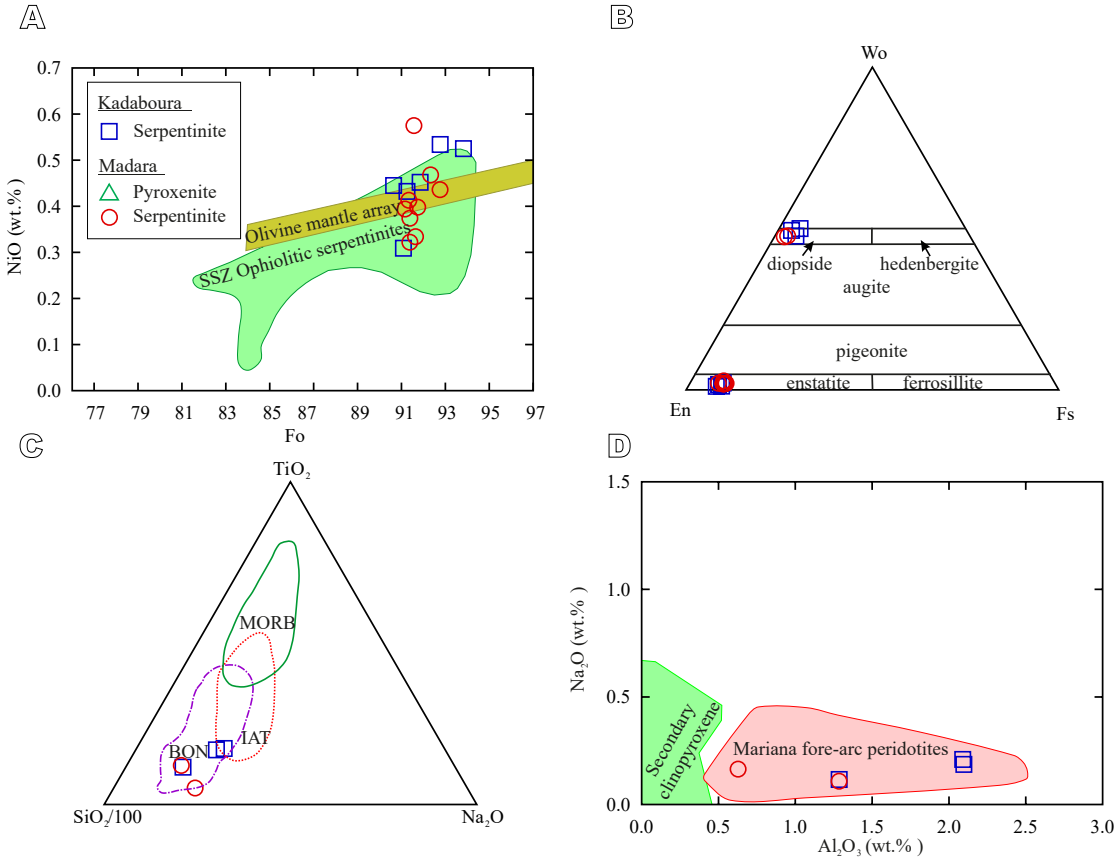

FIGURE 5. A) Olivine Fo and NiO (wt.%) contents compared with those from olivine mantle array (Takahashi, 1987) and from olivine in SZZ ophiolitic serpentinites of the EDE (Khalil and Azer, 2007). B) En-Wo-Fs pyroxene classification diagram (Morimoto *et al.*, 1988). C) SiO_2/100-TiO_2-Na_2O ternary diagram of clinopyroxene (Beccaluva *et al.*, 1989). Abbreviations: IAT= Island-Arc Tholeiite; MORB= normal Mid-Ocean Ridge Basalt; BON= boninite. D) Al_2O_3 vs. Na_2O diagram of clinopyroxene. Primary clinopyroxenes from the Mariana fore-arc peridotites (Ishii *et al.*, 1992; JunBing and ZhiGang, 2007; Murata *et al.*, 2009; Parkinson and Pearce, 1998) and secondary clinopyroxenes (JunBing and ZhiGang, 2007; Khedr and Arai, 2012; Kimball *et al.*, 1985; Murata *et al.*, 2009; Peacock, 1987) are shown for comparison.

2010). Clinopyroxenes are diopside (Fig. 5B) with compositions ranging from $En_{0.44}$ $Fs_{0.06}$ $Wo_{0.50}$ to $En_{0.50}$ $Fs_{0.03}$ $Wo_{0.47}$. They show high Mg# (89-95) similar to the unaltered clinopyroxene hosted in ophiolitic serpentinites from the CED of Egypt (Khedr and Arai, 2017). Moreover, the Al_2O_3 (0.63-2.10wt.%) and Cr_2O_3 (0.30-0.42 wt.%) contents are higher than those for the metamorphic clinopyroxene (mostly Al_2O_3<0.1 and Cr_2O_3<0.2 wt.%), revealing a primary nature (Nozaka, 2010). Their compositions match those in clinopyroxene of intra-oceanic fore-arc basin boninites (Fig. 5C). On the Al_2O_3 vs. Na_2O relationship, they are comparable to primary clinopyroxenes from the Mariana fore-arc peridotites (Fig. 5D).

Amphibole

Amphibole compositions show high MgO (21.46-24.06wt.%) and CaO (12.12-13.29wt.%) but low FeO (1.14-3.20wt.%) contents (Table V). According to Leake *et al.* (1997), they are classified as tremolite. Their Mg# is high and varies from 93 to 100. They have very low Ti (<0.1 apfu).

Serpentine

Serpentine minerals show a variation of MgO (23.16-44.38wt.%), Al_2O_3 up to 9.64wt.%, NiO up to 0.56wt.% and Cr_2O_3 up to 1.42wt.% contents (Table VI). Based on the MgO-SiO_2 diagram (Fig. 6A), they comprise pseudomorphic and antigorite serpentines, where nearly most of serpentines fall within the antigorite field. Moreover, most analyzed serpentines show very low Cr_2O_3 and Al_2O_3 contents comparable to those of mesh serpentines from the metamorphosed Sultan Complex, Washington (Fig. 6B). However, few serpentine analyses indicate bastite serpentines (Fig. 6B).

Chlorite

Chlorite compositions show a limited range of SiO_2 (26.63-30.93wt.%) and Al_2O_3 (16.34-19.98wt.%) contents but a wide range of FeO (5.10-17.16wt.%) and MgO (19.89-30.26wt.%) contents (Table VII). They show relatively high Cr_2O_3 contents (0.85-3.68wt.%). Their Si (apfu) and Fe/

Fe+Mg ratios correspond mainly to chlinochlore with few sheridanite and pycnochlorite (Hey, 1954).

Talc and carbonate

Talc contains mainly SiO_2 (52.06-69.93wt.%) and MgO (18.36-34.19 wt.%) (Table VIII). With increasing alteration, talc and serpentine minerals transform to carbonates. Carbonate analyses are listed in Table IX. They include calcite, magnesite and dolomite. Calcite is composed mainly of CaO (47.95-55.67wt.%) with low MgO (0.39-3.25wt.%) and FeO (0.18-0.89wt.%) contents. Magnesite consists mainly of MgO (39.92-45.32wt.%) with low CaO (0.12-0.27wt.%) and FeO (0.82-11.15wt%) contents. Dolomite shows high MgO (18.79-21.03wt.%) and CaO (31.25-35.03wt.%) and very low FeO (0.13-0.24wt.%) contents.

BULK-ROCK GEOCHEMISTRY

The bulk-rock geochemical data of the representative samples are given in Table 1. Major element oxides were normalized to an anhydrous basis and plotted on a volatile-free basis to diminish the variable element dilution associated with serpentinization. The studied rocks in both areas show variable LOI content (1.76-16.42wt.%; Table 1). Using normative compositions of olivine, orthopyroxene and clinopyroxene, most of the studied rocks are classified as harzburgite, and few as dunite and orthopyroxenite (Fig. 7A). Mantle rocks in Kadaboura area are serpentinites and serpentinized dunites, whereas in Madara area are serpentinites and serpentinized orthopyroxenites. The serpentinites in both areas seem to have harzburgitic compositions (Fig. 7A). All the studied rocks show high Mg# (90-94), like the other Neoproterozoic ophiolitic ultramafic rocks in the EDE (Ali *et al.*, 2021; Boskabadi *et al.*, 2017; Khalil and Azer, 2007). They exhibit depletion of Al_2O_3 and CaO and enrichment in MgO in comparison with the ultramafic cumulate and metamorphic peridotite of the ophiolite complexes (Fig. 7B). This Al_2O_3 and CaO depletion characterizes the ophiolitic ultramafic rocks in the EDE (Abdel-Karim *et al.*, 2016, 2018; Ali *et al.*, 2021; Azer and Khalil, 2005; Azer *et al.*, 2013). On the SiO_2/MgO vs. Al_2O_3 diagram (Fig. 7C), they plot in the ophiolitic peridotite field like other ophiolitic ultramafic rocks in the EDE.

Serpentinites of Kadaboura have low SiO_2 (41.82-44.67wt.%) and MgO (35.86-40.15wt.%) contents and high Al_2O_3 (2.72-4.34wt%) and CaO (3.78-5.81wt.%) contents compared with those of Madara (Table 1). The most refractory major element compositions are found in the Madara serpentinites (*i.e.* very low Al_2O_3 and CaO contents); a feature comparable to that of the refractory

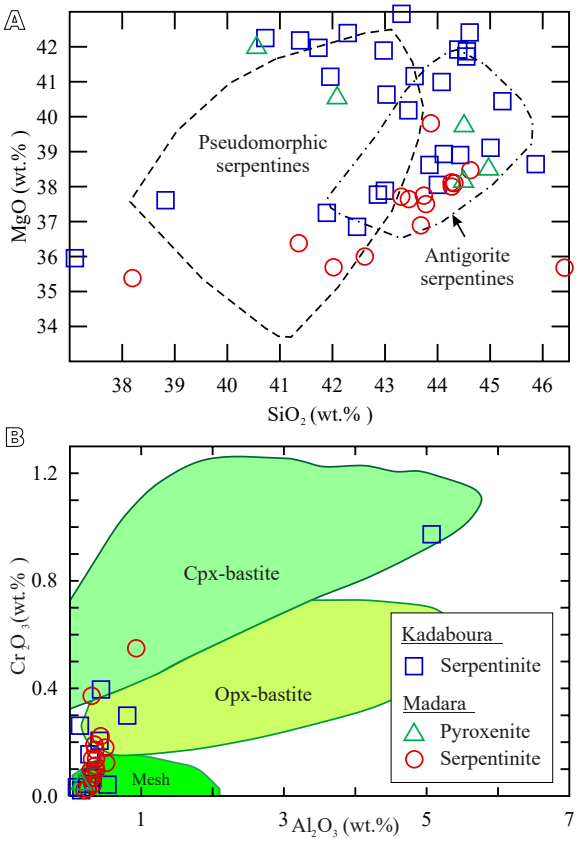

FIGURE 6. Serpentine composition diagrams: A) MgO vs. SiO_2, and B) Cr_2O_3 vs. Al_2O_3 (adapted from Dungan, 1979).

peridotites from the Trinity ophiolite in northern California (Gruau *et al.*, 1998) and modern fore-arcs (Ishii *et al.*, 1992). Moreover, the low CaO contents in Madara serpentinites resemble those observed on anhydrous abyssal and ophiolitic peridotites (Bodinier and Godard, 2003; Deschamps *et al.*, 2013; Niu, 2004).

Serpentinized dunites of Kadaboura have narrow ranges of SiO_2 (39.50-41.09wt.%), Al_2O_3 (2.75-3.70wt.%), CaO (4.77-6.10wt.%) and MgO (40.62-41.92wt.%) contents (Table 1). Their CaO contents are like those recorded in serpentinized dunites (up to 6.54wt.%) of subduction zone serpentinites (Deschamps *et al.*, 2013). They have low SiO_2 and Al_2O_3 contents and relatively high CaO and MgO contents compared with those of the associated serpentinites in the same area (Table 1).

Serpentinized orthopyroxenites of Madara have the highest SiO_2 (52.61-55.98wt.%) and the lowest Al_2O_3 (0.69-0.86wt.%) and MgO (33.11-36.17wt.%) contents compared with those of the other mantle rocks of both areas (Table 1). Their CaO contents (2.76-3.50wt.%) are higher than those of the associated serpentinites of the same area but lower than those of Kadaboura mantle rocks (Table 1).

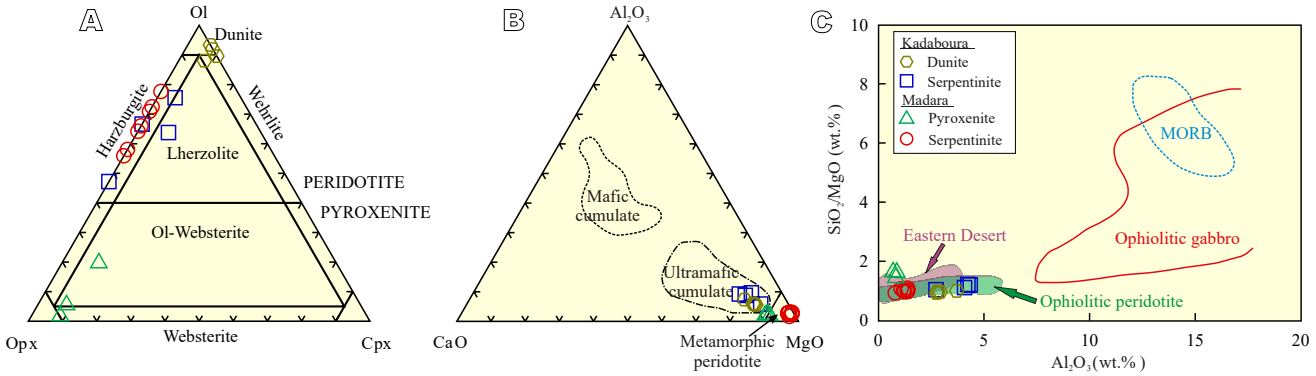

FIGURE 7. A) Normative Opx-Ol-Cpx composition diagram, and B) CaO-Al_2O_3-MgO ternary diagram (after Coleman, 1977). C) SiO_2/MgO vs. Al_2O_3 diagram. Fields of ophiolitic gabbro and peridotite as well as MORB are from Bodinier and Godard (2003). Data from the EDE are shown for comparison (Abdel-Karim *et al.*, 2016, 2018; Ali *et al.*, 2021; Azer and Khalil, 2005; Azer and Stern, 2007; Azer *et al.*, 2013; Zimmer *et al.*, 1995).

The compatible trace element contents (Cr= 2113-3425ppm, Ni= 1765-2756ppm) in Madara serpentinites are higher than those in Kadaboura mantle rocks (Table 1). The serpentinized orthopyroxenites of Madara (except sample A) have the lowest contents of Cr and Ni compared with those of the other mantle rocks of both areas (Table 1).

On the primitive mantle-normalized spider diagram (Fig. 8A), all the studied rocks display significant enrichment in U, Pb and P. The enrichment of these elements characterizes subduction zone serpentinites (Deschamps *et al.*, 2013). Excluding these elements, the trace element compositions are depleted relative to primitive mantle values (Fig. 8A). Except for serpentinized orthopyroxenite, we noticed decoupling between Nb and Ta, with a favored Ta enrichment (Fig. 8A) like that observed in subduction zone serpentinites (Deschamps *et al.*, 2013). The total REE concentrations are generally low (∑REE= 0.61-3.74) in all mantle rocks except in serpentinized orthopyroxenites which show a slight increase (∑REE= 11.42-13.69). Chondrite normalized REE patterns (Fig. 8B) of the studied rocks are generally relatively flat with variable Eu anomalies (Eu/Eu*= 0.41-4.43) and significant depletion in some HREE (*e.g.* Dy, Er and Yb). All rocks display LREE-enriched patterns [$(La/Sm)_N$= 1.08-8.07]; except two samples (A3 and A19) from Madara serpentinites which show low ratios [$(La/Sm)_N$= 0.57-0.58]. The ratios of $(Ce/Sm)_N$= 0.16-4.38 and Eu/Eu*= 0.41-4.43 in the studied rocks resemble those in the Trinity ophiolitic peridotites of northern California (Gruau *et al.*, 1998). The rocks also show low Ce/Pb (<1) and high Ba/Nb (up to 656) ratios.

DISCUSSION

Serpentinization process

The range of LOI content (1.76-16.42wt.%; Table 1) in the studied rocks indicates different degrees of post-magmatic alteration. Despite the mineralogical transformations occurred during the serpentinization process on peridotites, bulk-rock geochemical studies on subduction zone serpentinites, indicate, in general, negligible modifications of major elements (excluding Ca;

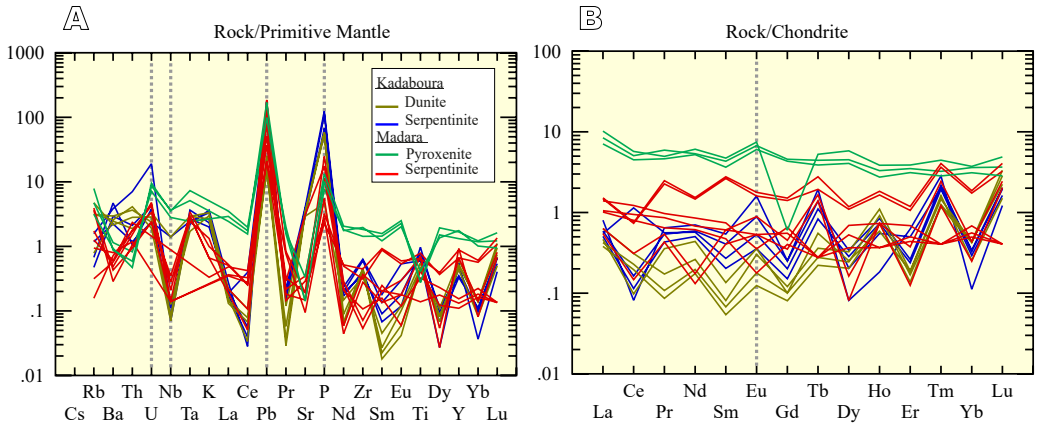

FIGURE 8. A) Primitive mantle-normalized trace element patterns. B) Chondrite-normalized REE patterns. The normalizing values are from Sun and McDonough (1989).

Deschamps *et al.*, 2013). Nevertheless, the studied rock samples show low CaO contents (0.15-6.10wt.%), excluding Ca adjustment during serpentinization. This inference is further reinforced by the irrelevant correlation between LOI and CaO contents in all rock samples (Fig. 9A). Moreover, the CaO contents of the studied rocks are within the range of subduction zone serpentinites (CaO= 0.00-13.09wt.%; Deschamps *et al.*, 2013). Likewise, the trace element compositions (excluding U and Sr) of subduction zone serpentinites generally show insignificant changes during serpentinization (*e.g.* Deschamps *et al.*, 2013; Paulick *et al.*, 2006). Though, U and Sr contents in the studied rocks also display irrelevant correlation with LOI (Fig. 9B, C). Generally, carbonate metasomatism of subduction zone serpentinites increases Pb, U and Sr (Deschamps *et al.*, 2013; Olivier and Boyet, 2006). In the studied rocks the Sr is not really enriched relative to primitive mantle (Fig. 8A), whereas the U and Pb are enriched in all samples even in those that are depleted in CaO (<2wt.%), arguing against the role of carbonate metasomatism in the bulk-rock budget of the studied rocks (*e.g.* Deschamps *et al.*, 2013). So, the serpentinization process in the studied rocks likely increased water contents without significant addition or removal of elements (*e.g.* Deschamps *et al.*, 2013). Thus, the bulk-rock chemistry of the studied rocks can help identifying their original protolith signatures (*e.g.* Chalot-Prat *et al.*, 2003; Deschamps *et al.*, 2013; Hattori and Guillot, 2007).

Metamorphic conditions

Serpentinization processes at low-temperatures yield early development of variably Fe-enriched chromites compared with mantle precursors due to Mg-Fe exchange with silicates and carbonates during invasion of fluids along cracks and around grain boundaries (Barnes, 2000; Gervilla *et al.*, 2012). Extra fluid invasion and reaction occurred at elevated temperatures inducing considerable chromite replacement by magnetite (Barnes, 2000; Gervilla *et al.*, 2012). In the studied rocks, altered chromite rims show higher FeO and lower Cr_2O_3, Al_2O_3 and MgO due to metamorphism compared to unaltered chromite cores (Table II). Furthermore, the plotting of Cr-rich magnetite rims on the Cr-Fe^{3+} join and neighboring Fe^{3+} apex (Fig. 4B) reveals an increase in Fe_2O_3 associated with a loss in Cr_2O_3 and Al_2O_3 during alteration. This increase in Fe_2O_3 indicates oxidation conditions during metamorphism (Anzil *et al.*, 2012). The development of Fe-rich chromite and Cr-rich magnetite rims around Al-rich chromite cores in the studied rocks indicates that the serpentinization processes started at low temperatures and continued to relatively elevated temperatures (Barnes, 2000).

Based on Figure 10A, the Al-rich chromite core compositions were equilibrated at temperatures mostly

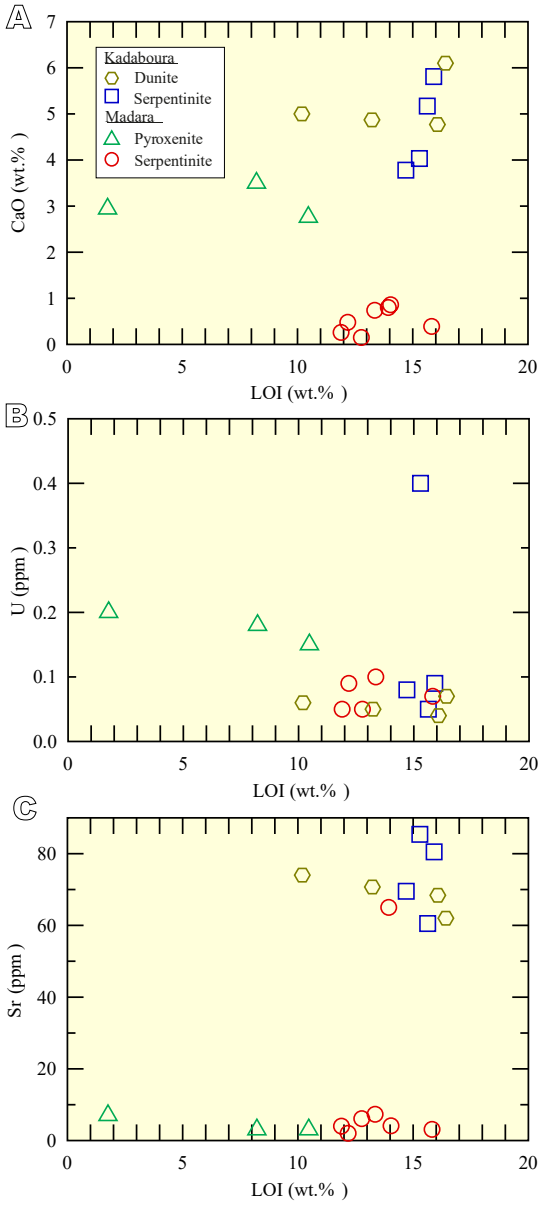

FIGURE 9. Plots showing comparison of LOI content with A) CaO, B) U and C) Sr.

below ~500 to 600°C. This temperature range is comparable to that estimated for primary magmatic chromite in greenschist up to lower amphibolite facies rocks (Barnes, 2000). Like in the Honeymoon Well in the northern Agnew–Wiluna Greenstone Belt, some Al-rich chromite core compositions fall outside the 600°C field of Sack and Ghiorso (1991), suggesting also primary magmatic compositions unaffected by metamorphic processes (Fig. 10A) (Barnes, 2000). Therefore, the Al-rich chromite cores reveal primary mantle compositions unaffected by metamorphism (*e.g.* Barnes, 2000). This implication is further supported by plotting Al-rich chromite core compositions in the primary chromite fields of greenschist

and lower amphibolite facies (Fig. 4B). Altered chromite rims show approximately pure magnetite compositions with very limited Cr-solubility, consistent with growth of magnetite at temperatures below 500°C (Fig. 10A; Barnes, 2000).

Mineralogical implications

The amphibole low Ti (<0.1 apfu) indicates metamorphic origin (Girardeau and Mevel, 1982). Serpentine mineral phases can be produced either by retrograde metamorphism of ultramafic rocks or by prograde metamorphism of the former serpentinites (Deer *et al.*, 1992). Usually, lizardites result from retrograde metamorphism, whereas antigorites arise during prograde metamorphism. Abundance of antigorite serpentines (Fig. 6A) suggests that the studied serpentinites were produced mainly in prograde metamorphism (Deer *et al.*, 1992). The presence of mesh serpentines reflects generation after olivine, whereas bastite is formed after pyroxene (Fig. 6B). Studies on natural and experimental samples (Allen and Seyfried, 2003; Martin and Fyfe, 1970; Mével, 2003) suggest that olivine transforms into serpentine at low temperatures (<300°C) at shallow depth, whereas orthopyroxene transforms into serpentine at high temperatures (>400°C) at deeper level during serpentinization. So, the prevalence of serpentine after olivine (Fig. 6B) in the studied rocks suggests formation mainly at temperatures below 300°C.

Chlorite compositions have relatively high Cr_2O_3 contents (0.85-3.68wt.%), likely reflecting formation after chromite as alteration products (Kodolanyi *et al.*, 2012). Accommodation of Al in the tetrahedral site (Al^{iv}) of chlorite structure is sensitive to temperatures of formation [*i.e.* T (°C)=106.2Al^{iv}+17.5; Cathelineau and Nieva, 1985]. Applying the geothermometer by Cathalineau and Nieva (1985) indicates that the studied chlorite formed at a temperature range between 215 and 289°C.

Nature of the mantle protolith and melting conditions

A good proxy to define the nature of the mantle and melting conditions is the Cr# of the unaltered chromite cores and the Fo contents of the coexisting olivine relicts in mantle rocks (Arai, 1994; Dick and Bullen, 1984; Hellebrand *et al.*, 2001). Abyssal peridotites and related serpentinites generated in slow spreading environments commonly have chromite with low Cr# (20<Cr#<60), suggesting that they are relatively fertile and represent residues from low degrees of melting (Michael and Bonatti, 1985). On the other hand, the subduction-related mantle rocks (comprising mantle wedge serpentinites) show chromite with high Cr# (>40), suggesting that they are highly depleted and refractory and represent residues from high degrees of melting (Dick and Bullen, 1984; Ozawa, 1994; Parkinson and Arculus, 1999). Thus, the high Cr# values (47-76) of the unaltered chromite cores in the studied serpentinites are consistent with subduction-related mantle rocks and reveal depleted nature and high degrees of melt extractions (Parkinson and Arculus, 1999). In addition to their higher Cr#, the Al_2O_3 contents range between 11.13 and 30.31wt.% comparable to those usually associated with hydrous melting in the mantle wedge above subduction zone (Dick and Bullen, 1984). The clinopyroxenes low TiO_2 contents (<1.0wt.%) suggest subalkaline nature (Le Bas, 1962). Moreover, their depletion in TiO_2 and Na_2O contents reflects oceanic origin (Delavari *et al.*, 2009); an inference supported by the high Mg# (90-94) of the host rocks which are comparable to those of oceanic peridotites (Bonatti and Michael, 1989).

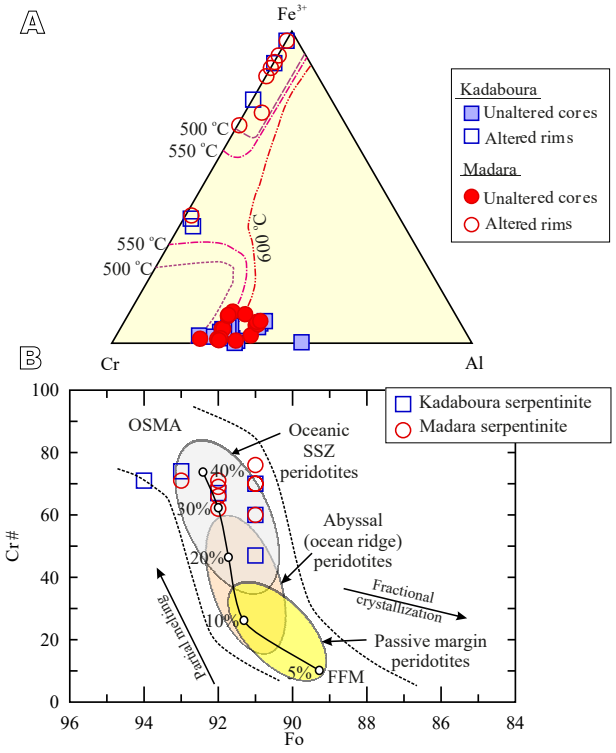

FIGURE 10. A) Chromite compositions from the studied mantle rocks compared with Sack and Ghiorso (1991) spinel stability fields for chromite and magnetite (after Barnes, 2000). B) Compositional relationship between Cr# of unaltered Al-rich chromite cores and Fo content of coexisting olivine relicts. The compositional fields of Olivine–Spinel Mantle Array (OSMA) and melting trend with Fertile MOR-type Mantle (FMM) are from Arai (1994). The passive margin, abyssal and SSZ peridotites are from Dick and Bullen (1984), Parkinson and Pearce (1998), Pearce *et al.* (2000) and Choi *et al.* (2008).

On the Fo-Cr# diagram (Fig. 10B), compositions of olivine relicts and Al-rich chromite cores of the studied serpentinites are plotted within the Olivine–Spinel Mantle Array (OSMA) and oceanic SSZ peridotites field, arguing for residual mantle origin. Accordingly, the studied serpentinites represent residual peridotites produced by high degrees of partial melting (mostly ~30-40%) of a

Fertile MORB Mantle (FMM) source and are refractory and depleted, having high Cr# and Fo contents (Fig. 10B). Compared to other ophiolitic serpentinites in the EDE, the estimated degrees of partial melting are similar to those of fore-arc serpentinites from G. El-Maiyit (23-35%), but higher than those of MOR-type serpentinites from Um El-Saneyat (15-20%) and MOR-arc transition serpentinites from W. Atalla (18-25%) (Gamal El Dien *et al.*, 2016). Moreover, the range of melt extraction lies within the range of SSZ peridotites (15-40%; Mellini *et al.*, 2005; Pearce *et al.*, 2000) but higher than that in abyssal peridotites (10-20%; Dick and Bullen, 1984) and passive margin peridotites (5-15%; Pearce *et al.*, 2000).

The less mobile trace element contents (*e.g.* Co, V, and Zn) in the studied rocks indicate that they were possibly derived from a harzburgite-dunite protolith (Fig. 11A) like Fawakhir, Abu Fannani and Barramiya serpentinites in the CED of Egypt (Surour, 2017). Depletion in most of the trace element compositions relative to the primitive mantle values reflects a residual origin of their mantle protolith (Fig. 8A; Sun and McDonough, 1989). Almost all the studied samples have low Al_2O_3 and CaO contents (Table 1), reflecting nearly absence of clinopyroxene in their mantle peridotite protolith (Dick and Bullen, 1984). These low values also suggest depleted mantle source (Bonatti and Michael, 1989). The high Mg# along with the high Ni and Cr contents and the low incompatible trace elements are in accordance with the depleted and highly refractory nature of the mantle protolith (Abdel-Karim *et al.*, 2016; Khalil, 2007; Parkinson and Pearce, 1998; Roberts, 1992).

The Al_2O_3 contents of the studied rocks are comparable to those in modern fore-arc peridotites and Neoproterozoic fore-arc ophiolites (Fig. 11B). Madara serpentinites show low Al_2O_3/SiO_2 ratios (<0.03), resembling fore-arc mantle wedge serpentinites (Fig. 11C) (Deschamps *et al.*, 2013). This inference reveals that their mantle protolith had suffered a melting extraction event before serpentinization that show no effect on the Al_2O_3/SiO_2 ratios (Deschamps *et al.*, 2013;

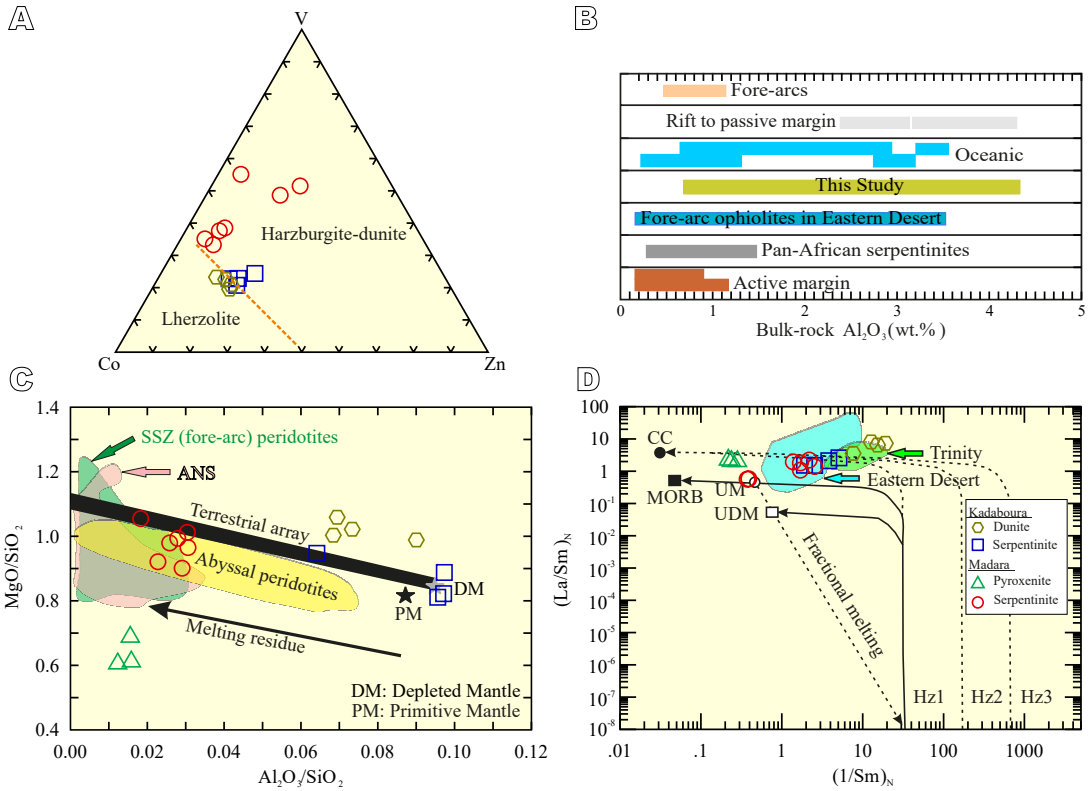

FIGURE 11. A) Co-Y-Zn ternary diagram (Pfeifer, 1979). B) Bulk-rock Al_2O_3 (wt.%) content of the studied rocks compared with those from other tectonic settings (Floyd, 1991). Data source: Pan-African serpentinites (Abdel-Karim and Ahmed, 2010; El Bahariya and Arai, 2003); fore-arc ophiolites from the Eastern Desert of Egypt (Abdel-Karim *et al.*, 2016, 2018; Ali *et al.*, 2021). C) MgO/SiO_2 vs. Al_2O_3/SiO_2 diagram. Primitive and depleted mantle values are from McDonough and Sun (1995) and Salters and Stracke (2004), respectively. The "terrestrial array" represents the bulk silicate Earth evolution (Jagoutz *et al.*, 1979; Hart and Zindler, 1986). Fields of abyssal and fore-arc peridotite are after Parkinson and Pearce (1998), Pearce *et al.* (2000) and Niu (2004). The ANS ophiolitic peridotite field is after Ahmed and Habtoor (2015), Abdel-Karim *et al.* (2018), and Ali *et al.* (2021). D) Chondrite-normalized $(La/Sm)_N$ vs. $(1/Sm)_N$ diagram (after Sharma and Wasserburg, 1996). MORB: Mid-Ocean Ridge Basalts; UM: Upper Mantle composition; UDM: Ultra-Depleted Melt composition; CC: Continental Crust composition; Hz1, Hz2 and Hz3 model harzburgite compositions. Fields of the ophiolitic ultramafic rocks from the EDE (Abdel-Karim *et al.*, 2016, 2018; Ali *et al.*, 2021) and the Trinity in northern California (Gruau *et al.*, 1998) are shown for comparison.

Paulick *et al.*, 2006; Snow and Dick, 1995). Their low MgO/SiO_2 ratios (<1.1; Fig. 11C) are like those in serpentinized harzburgite of subduction zone serpentinites (Deschamps *et al.*, 2013). Moreover, the Al_2O_3/SiO_2 and MgO/SiO_2 ratios overlap the fields of the ANS and SSZ peridotites developed in a fore-arc basin (Fig. 11C). Kadaboura serpentinites have Al_2O_3/SiO_2 and MgO/SiO_2 ratios consistent with depleted mantle values except the serpentinite sample (95/17) that follows the terrestrial mantle array (Fig. 11C). Kadaboura serpentinized dunites plot above the terrestrial mantle array (Fig. 11C), suggesting an increase in the olivine/orthopyroxene ratios (Deschamps *et al.*, 2013). On the other hand, the serpentinized orthopyroxenites of Madara plot below the terrestrial mantle array (*i.e.* lower MgO/SiO_2 ratios; Fig. 11C), likely due to the pre-serpentinization lithology variation (*i.e.* orthopyroxenite; Fig. 7A). Generally, the sample shift from the mantle array is likely related to lithological variations (*e.g.* pyroxenite, dunite) or weathering of seafloor (Kodolanyi *et al.*, 2012).

Modification of the mantle source

The depleted nature of the mantle source of the ophiolite complexes can be modified by contamination, which generally could happen during the evolution of the mantle in the SSZ environment (Delavari *et al.*, 2009; Gruau *et al.*, 1998). It is also possible that the contamination arises during or after the ophiolite emplacement onto the continent (Sharma and Wasserburg, 1996).

On the $(La/Sm)_N$ vs. $(1/Sm)_N$ diagram (Fig. 11D), the studied mantle rocks are compared with model peridotite formed by contamination of the residual harzburgite by MORB melts or continental materials (Sharma and Wasserburg, 1996). Only two samples (A3 and A19) from Madara serpentinites, with LREE-depletion [$(La/Sm)_N<1$], plot on the solid curve (Hz1-MORB), suggesting that their harzburgitic mantle was likely contaminated with MORB-like melt (Sharma and Wasserburg, 1996). So, they possibly formed through MORB melt/mantle rock reaction process like serpentinized peridotites from the Gerf ophiolitic ultramafic rocks of the SED of Egypt (Abdel-Karim *et al.*, 2016). On the other hand, the rest of the mantle rocks from both areas, with LREE-enrichment [$(La/Sm)_N>1$], plot nearby and on the dashed curves tracking contamination of their harzburgitic mantle by continental materials (crustal and/or subduction components) (Fig. 11D). They overlap the fields of mantle rocks from the EDE and the Trinity in the northern California (Fig. 11D). The evolution of the studied mantle rocks in a SSZ setting possibly caused contamination of their residual depleted mantle through interaction with melts/fluids produced from the subducted materials (*e.g.* Sharma and Wasserburg, 1996 and references therein). Their low Ce/Pb and high Ba/Nb ratios along with the enrichment of U, Pb and P further confirm subduction contribution (*e.g.* Deschamps *et al.*, 2013; Yang and Zhou, 2009). The same conclusion was supposed to elucidate the origin of some ophiolitic ultramafic rocks in the EDE (Abdel-Karim *et al.*, 2016, 2018; Ali *et al.*, 2021). The origin of the Trinity ophiolitic ultramafic rocks in northern California is explained by contamination of their mantle peridotite source by crustal materials (Gruau *et al.*, 1998). The ophiolitic ultramafic rocks (including the studied rocks) of the EDE exhibit variable LREE-enrichment (Fig. 11D), probably indicating variable input of subduction components into the mantle source.

Origin of the orthopyroxenite

Origin of the orthopyroxenites in the ophiolite mantle section is commonly attributed to the interaction between mantle peridotites and subducted components (Berly *et al.*, 2006). Also, they may possibly be generated by interaction of the mantle wedge peridotites with high-SiO_2 melts (Arai *et al.*, 2006).

The ANS mantle portion is commonly represented by extremely depleted harzburgites (Stern *et al.*, 2004). Melting such extremely depleted mantle under hydrous conditions can produce boninitic melts, which are considered to represent the parental magma source of the orthopyroxenite (Müntener *et al.*, 2001; Python *et al.*, 2008). Orthopyroxenites have been hardly reported in the ophiolite complexes of the EDE. They are only recorded in Kurbiyay, Hammariya, Bir Al-Edeid, Mudarjaj and Gerf ophiolite complexes (Abdel-Karim *et al.*, 2008, 2016; Ahmed *et al.*, 2012; Azer and Khalil, 2005; Gahlan and Arai, 2009). The origin of the orthopyroxenites in Mudarjaj ophiolite complex in the SED of Egypt was attributed to contamination of their arc-related melts by crustal rocks (Ahmed *et al.*, 2012). Moreover, orthopyroxenites in the Gerf ophiolite complex in the SED of Egypt were produced through contamination of their mantle source by subduction-related components (Abdel-Karim *et al.*, 2016).

The studied orthopyroxenites in Madara have serpentine chemistry analogous to those hosted in the associated serpentinites (Fig. 6). Moreover, their SiO_2/MgO ratios and Al_2O_3 contents are like those of the associated serpeninites (Fig. 7C). They plot close to the ophiolitic peridotites field and overlap the field of ophiolitic ultramafic rocks of the EDE (Fig. 7C). These inferences reveal a co-genetic nature. Overall, the trace element patterns (Fig. 8) of the Madara orthopyroxenites and the associated serpentinites are comparable, supporting the co-genetic origin. Moreover, the studied orthopyroxenites have very low TiO_2 contents (Table 1), suggesting re-melting of an extremely depleted mantle peridotite source (Sun and Nesbitt, 1978). They show negative Nb and Ti anomalies, and enrichment in

Large-Ion Lithophile Element (LILE) (*e.g.* Rb, P, Pb) and LREE (Fig. 8) revealing subduction signatures. Accordingly, the origin of the Madara orthopyroxenites can be attributed to interaction of their depleted harzburgite mantle source with melts/fluids produced from the subducted slab during evolution of the mantle in a SSZ setting (Fig. 11D).

Geodynamic evolution

The Gondwana supercontinent assembly and breakup include various complex processes that generate major changes in the geochemical characteristics of the ANS mantle (Abu-Alam *et al.*, 2013; Ali *et al.*, 2023; Gamal El Dien *et al.*, 2016; Stern *et al.*, 2004). These complex processes incorporate melting, depletion, and metasomatic enrichment of the upper mantle peridotites (Abdel-Karim *et al.*, 2016; Ali *et al.*, 2023; Gahlan *et al.*, 2018, 2020; Gamal El Dien *et al.*, 2016; Stern *et al.*, 2004). Mineralogical and geochemical studies indicate that the evolution history of the Neoproterozoic mantle peridotites in the ANS have several origins and tectonic settings, implying generation during various episodes (Abdel-Karim *et al.*, 2016; Ali *et al.*, 2021; Azer *et al.*, 2019; El Bahariya, 2018; Gamal El Dien *et al.*, 2016; Zimmer *et al.*, 1995). In the early stage of evolution during the opening of the Mozambique Ocean between East and West Gondwana (Fig. 12A), the Neoproterozoic mantle in the ANS underwent anhydrous melting forming MOR-type abyssal mantle peridotites (*e.g.* Um El-Saneyat peridotites in the EDE; Gamal El Dien *et al.*, 2016). The collision between East and West Gondwana results in closing of the Mozambique Ocean and beginning of the subduction stage (Jöns and Schenk, 2007; Fig. 12B). In the subduction initiation stage (Fig. 12B), the early formed abyssal peridotites are subsequently introduced into the subduction zone. The emplacement of the abyssal mantle peridotites into the subduction zone may trigger further melting forming more refractory harzburgites (*e.g.* G. El-Maiyit and W. Atalla in the EDE; Gamal El Dien *et al.*, 2016). These harzburgites probably underwent variable metasomatic enrichment due to the uprising melts/hydrothermal fluids from the sub-arc region. The fluid amount produced from the dehydration of the subducted slab in the incipient-arc (*i.e.* proto-fore-arc; Fig. 12B) stage is trivial (*e.g.* Whattam and Stern, 2011). According to Gamal El Dien *et al.* (2016), the W. Atalla peridotites were formed by moderate degrees of melting in a transitional MOR-arc setting. During the mature arc stage (*i.e.* true subduction; Fig. 12C), large amounts of slab-derived fluids were produced causing intensive melting in the mature arc mantle (*e.g.* Stern *et al.*, 2004; Whattam and Stern, 2011). In this stage, the most refractory peridotites (*e.g.* G. El Maiyit) are produced because of high degrees partial melting in a SSZ environment (Gamal El Dien *et al.*, 2016). It seems that the Neoproterozoic mantle of the ANS underwent advanced stages of hydrous melting, extreme depletion, and enrichments in a SSZ setting (*e.g.* Gamal El Dien *et al.*, 2016). We suggest that the studied mantle rocks, which are highly refractory and are produced after high degrees partial melting (mostly ~30-40%) of the sub-fore-arc mantle, belong to the mature arc stage (Fig. 12C) (*e.g.* Gamal El Dien *et al.*, 2016). The presence of MOR- and SSZ-type peridotites in the Neoproterozoic ophiolite complexes of the Egyptian Eastern Desert of the ANS indicates transitional geodynamic evolutionary history of the Precambrian lithosphere of the Mozambique Ocean (Abdel-Karim *et al.*, 2021; El Bahariya, 2018; Gamal El Dien *et al.*, 2016).

In summary, the seafloor spreading of the Mozambique Ocean produced an oceanic lithosphere that afterwards was emplaced in the upper plate of the intra-oceanic subduction zone (*i.e.* SSZ environment), in which the formerly depleted Neoproterozoic mantle in the ANS underwent mature stages of hydrous melting, extreme depletion, and enrichment.

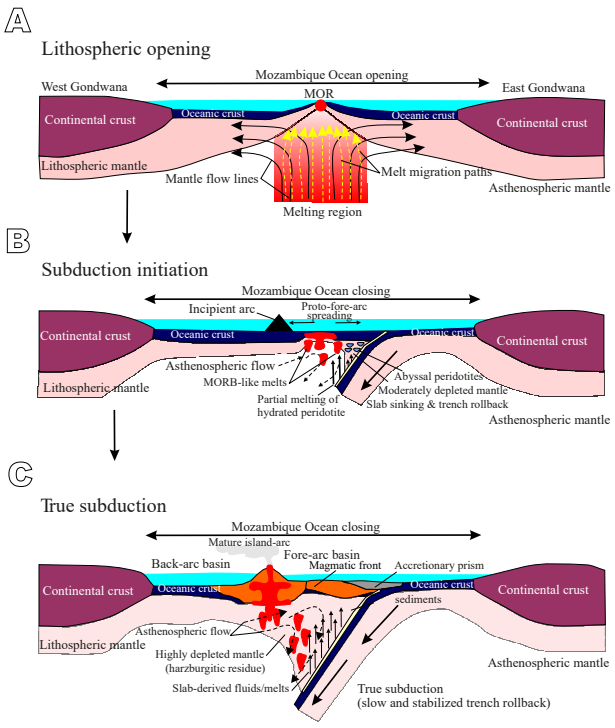

FIGURE 12. Tectonic model suggested for the evolution of the studied mantle rocks in the ANS (modified after Whattam and Stern, 2011; Gamal El Dien *et al.*, 2016). A) Mozambique Ocean opening between East and West Gondwana. B) Subduction initiation stage (*i.e.* incipient arc), in which partial melting is triggered in the mantle wedge during Mozambique oceanic crust subduction beneath fore-arc region. The model also shows spreading centers formation (*i.e.* proto-fore-arc) over the subduction zone. C) True subduction stage (*i.e.* mature-arc), in which enormous slab-derived fluids were produced leading to high degrees of partial melting and formation of the most refractory peridotites. The studied mantle rocks are interpreted to have formed during this stage.

CONCLUSIONS

The studied mantle rocks from Kadaboura and Madara areas belong to the ophiolite complexes in the EDE. Kadaboura mantle rocks consist of serpentinites and serpentinized dunites, whereas those of Madara comprise serpentinites and serpentinized orthopyroxenites.

The unaltered chromite core compositions were equilibrated at temperatures mostly <500-600°C, which are comparable to those estimated for the primary magmatic chromite in the greenschist up to lower amphibolite facies rocks. The high Cr# of the unaltered chromite cores and the Mg-rich nature of the olivine relicts suggest that the studied rocks were generated from extremely depleted mantle residues after high melting degrees, mostly between ~30 and 40%, comparable to those estimated for the SSZ peridotites. Moreover, the clinopyroxene relicts exhibit compositions similar to those of the Mariana fore-arc peridotites.

The studied mantle rocks show geochemical features that support derivation from an extremely depleted mantle source. Modeling of REEs suggests that the origin of the studied mantle rocks can be explained by the interaction of highly depleted harzburgitic mantle residues with melts/fluids derived from the subducted slab during their evolution in a fore-arc basin of the SSZ setting.

The proposed geodynamic model suggests that the oceanic lithosphere formed during the Mozambique Ocean seafloor spreading was emplaced in the upper plate of the intra-oceanic subduction zone (*i.e.* SSZ environment), in which the formerly depleted Neoproterozoic ANS mantle experienced mature phases of hydrous melting, extreme depletion and enrichment.

ACKNOWLEDGMENTS

The valuable comments, suggestions and corrections given by I.F. Blanco-Quintero and an anonymous referee are greatly acknowledged. Also, the authors would like to express their great appreciation to the Guest Editor.

REFERENCES

Abd El-Rahman, Y., Helmy, H.M., Shibata, T., Yoshikawa, M., Arai, S., Tamura, A., 2012. Mineral chemistry of the Neoproterozoic Alaskan-type Akarem Intrusion with special emphasis on amphibole: Implications for the pluton origin and evolution of subduction-related magma. Lithos, 155, 410-425.

Abdallah, S.E., Ali, S., Obeid, M.A., 2019. Geochemistry of an Alaskan-type mafic-ultramafic complex in Eastern Desert, Egypt: New insights and constraints on the Neoproterozoic island arc magmatism. Geoscience Frontiers, 10(3), 941-955. DOI:10.1016/j.gsf.2018.04.009

Abdel Halim, A., Helmy, H.M., Abdel-Rahman, Y.M., Shibata, T., El-Mahallawi, M.M., Yoshikawa, M., Arai, S., 2016. Petrology of the Motaghairat mafic–ultramafic complex, Eastern Desert, Egypt: a high-Mg post-collisional extension-related layered intrusion. Journal of Asian Earth Sciences, 116, 164-180.

Abdel-Karim, A.M., Hemimi, Z., El-Sherbenyi, A.T., 1997. Petrology and geochemistry of Umm Battat younger gabbros, central Eastern Desert, Egypt. Egyptian Journal of Geology, 41/2B, 605-625.

Abdel-Karim, A.M., Soliman, M.M., El-Kazzaz, Y., Mazhar, A.A., Abdel-Gawad, G.A., 2001. Geological and geochemical characteristics of the mafic–ultramafic rocks of Gabal Garf area, south Eastern Desert, Egypt. Annals of the Geological Survey of Egypt, XXIV, 193-218.

Abdel-Karim, A.M., Azzaz, S.A., Moharem, A.F., El-Alfy, H., 2008. Petrological and geochemical studies on the ophiolite and island arc association of Wadi Hammaryia, Egypt. Arabian Journal for Science and Engineering, 33(1C), 117-138.

Abdel-Karim, A.M., Ahmed, Z., 2010. Possible origin of the ophiolites of Eastern Desert of Egypt, from geochemical prospectives. Arabian Journal for Science and Engineering, 34, 1-27.

Abdel-Karim, A.M., Ali, S., Helmy, H.M., El-Shafei, S.A., 2016. Fore-arc setting of the Gerf ophiolite, Eastern Desert, Egypt: evidence from mineral chemistry and geochemistry of ultramafites. Lithos, 263, 52-65.

Abdel-Karim, A.M., Ali, S., El-Shafei, S.A., 2018. Mineral chemistry and geochemistry of ophiolitic metaultramafics from Um Halham and Fawakhir, Central Eastern Desert, Egypt International Journal of Earth Sciences, 107, 2337-2355. DOI: 10.1007/s00531-018-1601-2

Abdel-Karim, A.M., El-Shafei, S.A., Azer M.K., 2021. The Neoproterozoic ophiolitic ultramafic rocks in Eastern Desert of Egypt: implications for petrogenesis and metasomatic processes. Internal Geology Review, 92, 1-25. DOI: 10.1080/00206814.2019.1708816

Abu-Alam, T.S., Santosh, M., Brown, M., Stüwe, K., 2013. Gondwana collision. Mineralogy and Petrology, 107, 631-634.

Abu El-Ela, A.M., 1996. Contribution to mineralogy and geochemistry of some serpentinites from the Eastern Desert of Egypt. Middle East Research Center. Ain Shams University, Earth Science, 10, 1-25.

Abuamarah, B.A., Asimow, P.D., Azer, M.K., Ghrefat, H., 2020. Suprasubduction-zone origin of the podiform chromitites of the Bir Tuluhah ophiolite, Saudi Arabia, during Neoproterozoic assembly of the Arabian Shield. Lithos, 360-361, 105439.

Ahmed, A.A., 1991. Ultrabasic and basic intrusions of Um Ginud and Motaghairat area, South Eastern Desert, Egypt. Bulletin of the Faculty of Science-Assuit University, 20, 183-213.

Ahmed, A.H., Gharib, M.E., Arai, S., 2012. Characterization of the thermally metamorphosed mantle–crust transition zone

of the Neoproterozoic ophiolite at Gebel Mudarjaj, south Eastern Desert, Egypt. Lithos, 142-143, 67-83.

Ahmed, A.H., Habtoor, A., 2015. Heterogeneously depleted Precambrian lithosphere deduced from mantle peridotites and associated chromitite deposits of Al'Ays ophiolite, Northwestern Arabian Shield, Saudi Arabia. Ore Geology Reviews, 67, 279-296.

Ali, K.A., Azer, M.K., Gahlan, H.A., Wilde, S.A., Samuel, M.D., Stern, R.J., 2010. Age constraints on the formation and emplacement of Neoproterozoic ophiolites along the Allaqi Suture, south Eastern Desert, Egypt. Gondwana Research, 18, 583-595.

Ali, S., Abart, R., Sayyed, M.I., Hauzenberger, C.A., Sami, M., 2023. Petrogenesis of the Wadi El-Faliq Gabbroic Intrusion in the Central Eastern Desert of Egypt: Implications for Neoproterozoic Post-Collisional Magmatism Associated with the Najd Fault System. Minerals, 13 (1), 10. https://doi.org/10.3390/min13010010

Ali, S., Ntaflos, T., Sami, M., 2021. Geochemistry of Khor Um-Safi ophiolitic serpentinites, central Eastern Desert, Egypt: Implications for Neoproterozoic arc-basin system in the Arabian-Nubian Shield. Geochemistry, 81(1), 125690. DOI: 10.1016/j.chemer.2020.125690

Allen, D.E., Seyfried, Jr., E., 2003. Compositional controls on vent fluids from ultramafic-hosted hydrothermal systems at mid-ocean ridges: an experimental study at 400ºC, 500 bars. Geochimica et Cosmochimica Acta, 67(8), 1531-1542.

Anzil, P.A., Guereschi, A.B., Martino, R.D., 2012. Mineral chemistry and geothermometry using relict primary minerals in the La Cocha ultramafic body: a slice of the upper mantle in the Sierra Chica of Cordoba, Sierras Pampeanas, Argentina. Journal of South America Earth Science, 40, 38-52.

Arai, S., 1994. Characterization of spinel peridotites by olivine–spinel compositional relationships: review and interpretation. Chemical Geology, 113, 191-204.

Arai, S., Kadoshima, K., Morishita, T., 2006. Widespread arc-related melting in the mantle section of the northern Oman ophiolite as inferred from detrital chromian spinels. Journal of the Geological Society, 163, 869-879.

Azer, M.K., Khalil, A.E.S., 2005. Petrological and mineralogical studies of Pan-African serpentinites at Bir Al-Edeid area, central Eastern Desert, Egypt. Journal of African Earth Sciences, 43, 525-536.

Azer, M.K., Stern, R.J., 2007. Neoproterozoic (835-720 Ma) serpentinites in the Eastern Desert, Egypt: fragments of forearc mantle. Geology, 115, 457-472.

Azer, M.K., El-Gharbawy, R.I., 2011. Contribution to the Neoproterozoic layered mafic-ultramafic intrusion of Gabal Imleih, south Sinai, Egypt: Implication of post-collisional magmatism in the north Arabian-Nubian Shield. Journal of African Earth Sciences, 60, 253-272.

Azer, M.K., Samuel, M.D., Ali, K.A., Gahlan, H.A., Stern, R.J., Ren, M., Moussa, H.E., 2013. Neoproterozoic ophiolitic peridotites along the Allaqi–Heiani Suture, South Eastern Desert, Egypt. Mineralogy and Petrology, 107(5), 829-848.

Azer, M.K., Obeid, M.A., Gahlan, H.A., 2016. Late Neoproterozoic layered mafic intrusion of arc-affinity in the Arabian-Nubian Shield: A case study from the Shahira layered mafic intrusion, southern Sinai, Egypt. Geologica Acta, 14(3), 237-259.

Azer, M.K., Gahlan, H.A., Asimow, P.D., Al-Kahtany, K.M., 2017. The Late Neoproterozoic Dahanib mafic-ultramafic intrusion, South Eastern Desert, Egypt: is it an Alaskan-type or a layered intrusion? American Journal of Science, 317, 901-940.

Azer, M.K., Gahlan, H.A., Asimow, P.D., Mubarak, H.S., Al-Kahtany, K.M., 2019. Multiple stages of carbonation and element redistribution during formation of ultramafic-hosted magnesite in Neoproterozoic ophiolites of the Arabian-Nubian Shield, Egypt. Journal of Geology, 127, 81-107.

Barnes, S.I., 2000. Chromite in komatiites, II. Modification during greenschist to mid-amphibolite facies metamorphism. Journal of Petrology, 41(3), 387-409.

Barnes, S.J., Roeder, P.L., 2001. The range of spinel compositions in terrestrial mafic and ultramafic rocks. Journal of Petrology, 42(12), 2279-2302.

Beccaluva, L., Macciota, G., Piccardo, G.B., Zeda, O., 1989. Clinopyroxene composition of ophiolitic basalts as petrogenetic indicator. Chemical Geology, 77, 165-182.

Berly, T.J., Hermann, J., Arculus, R.J., Lapierre, H., 2006. Supra-subduction zone pyroxenites from San Jore and Santa Isabel (Solomon Islands). Journal of Petrology, 47, 1531-1555.

Bodinier, J.L., Godard, M., 2003. Orogenic, ophiolitic, and abyssal peridotites. In: Carlson, R.W. (ed.). The Mantle and Core: Treatise on Geochemistry. Amsterdam, Elsevier Science Ltd., 2nd edition, 103-170.

Bonatti, E., Michael, P.J., 1989. Mantle peridotites from continental rifts to oceanic basins to subduction zones. Earth and Planetary Science Letters, 91, 297-311.

Boskabadi, A., Pitcairn, I.K., Broman, C., Boyce, A., Teagle, D.A.H., Cooper, M.J., Azer, M.K., Stern, R.J., Mohamed, F.H., Majka, J., 2017. Carbonate alteration of ophiolitic rocks in the Arabian–Nubian Shield of Egypt: sources and compositions of the carbonating fluid and implications for the formation of Au deposits. International Geology Review, 59(4), 391-419.

Cathelineau, M., Nieva, D., 1985. A chlorite solid solution geothermometer the Los Azufres (Mexico) geothermal system. Contribution to Mineralogy and Petrology, 91, 235-244. DOI: 10.1007/BF00413350

Chalot-Prat, F., Ganne, J., Lombard, A., 2003. No significant element transfer from the oceanic plate to the mantle wedge during subduction and exhumation of the Tethys lithosphere (Western Alps). Lithos, 69, 69-103.

Choi, S.H., Shervais, J.W., Mukasa, S.B., 2008. Supra-subduction and abyssal mantle peridotites of the coast range ophiolite, California. Contributions to Mineralogy and Petrology, 156, 551-576.

Coleman, R.G., 1977. Ophiolites. Berlin, Springer-Verlag, 229pp.

Deer, W.A., Howie, R.A., Zussman, J., 1992. An introduction to the rock forming minerals. London, Longman Scientific and Technical, 2nd edition, 696pp.

Delavari, M., Amini, S., Saccani, E., Beccaluva, L., 2009. Geochemistry and petrogenesis of mantle peridotites from

the Nehbandan Ophiolitic Complex, eastern Iran. Journal of Applied Science, 9(15), 2671-2687.

Deschamps, F., Godar, M., Guillot, S., Hattori, K., 2013. Geochemistry of subduction zone serpentinites: a review. Lithos, 178, 96-127.

Dick, H.B., Bullen, T., 1984. Chromian spinel as a petrogenetic indicator in abyssal and Alpine-type peridotites and spatially associated lavas. Contribution to Mineralogy and Petrology, 86, 54-76.

Dixon, T.H., 1981. Gebel Dahanib, Egypt: a late Precambrian layered sill of komatiitic composition. Contributions to Mineralogy and Petrology, 76, 42–52.

Dungan, M.A., 1979. A microprobe study of antigorite and some serpentine pseudomorphs. Canadian Mineralogist, 17, 711-784.

El Bahariya, G.A., 2018. Classification of the Neoproterozoic ophiolites of the Central Eastern Desert, Egypt based on field geological characteristics and mode of occurrence. Arabian Journal of Geosciences, 11, 313pp. DOI: 10.1007/s12517-018-3677-1

El Bahariya, G.A., Arai, S., 2003. Petrology and origin of Pan-African serpentinites with particular reference to chromian spinel compositions, Eastern Desert, Egypt: implication for supra-subduction zone ophiolite. Third International Conference on the Geology of Africa, Egypt, Assiut University, 371-388.

El-Sayed, M.M., Furnes, H., Mohamed, F.H., 1999. Geochemical constraints on the tectonomagmatic evolution of the late Precambrian Fawakhir ophiolite, central Eastern Desert, Egypt. Journal of African Earth Science, 29, 515-533.

El-Sharkawy, M.A., El-Bayoumi, R., 1979. The ophiolites of Wadi Ghadir area, Eastern Desert, Egypt. Annal Geological Survey Egypt, 9, 125-135.

Engin, T., Balci, M., Sümer, Y., Özkan, Y.Z., 1980. Guleman (Elazig) krom yataklari ve peridotit biriminin genel jeolojik konumu ve yapisal özellikleri. Maden Tetkik ve Arama Dergisi, 95-96, 77-101.

Evans, B., Frost, B., 1975. Chrome spinel in progressive metamorphism: a preliminary analysis. Geochimica et Cosmochimica Acta, 39, 379-414.

Farahat, E.S., Helmy, H.M., 2006. Abu Hamamid Neoproterozoic Alaskan-type complex, south Eastern Desert, Egypt. Journal of African Earth Sciences, 45, 187-197.

Farahat, E.S., Hoinkes, G., Mogessie, A., 2011. Petrogenetic and geotectonic significance of Neoproterozoic suprasubduction mantle as revealed by the Wizer ophiolite complex, Central Eastern Desert, Egypt. International Journal of Earth Sciences, 100, 1433-1450.

Floyd, P.A., 1991. Oceanic basalts. New York, Blachie and Son Ltd, 456pp.

Gahlan, H.A., Arai, S., 2009. Carbonate-orthopyroxenite lenses from the Neoproterozoic Gerf ophiolite, South Eastern Desert, Egypt: The first record in the Arabian Nubian shield ophiolites. Journal of African Earth Sciences, 53, 70-82. DOI: 10.1016/j.jafrearsci.2008.09.005

Gahlan, H.A., Azer, M.K., Khalil, A.E.S., 2015. The Neoproterozoic Abu Dahr ophiolite, South Eastern Desert, Egypt: Petrological characteristics and tectonomagmatic evolution. Mineralogy and Petrology, 109, 611-630.

Gahlan, H.A., Azer, M.K., Asimow, P.D., 2018. On the relative timing of listwaenite formation and chromian spinel equilibration in serpentinites. American Mineralogist, 103, 1087-1102.

Gahlan, H.A., Azer, M.K., Asimow, P.D., Mubarak, H.S., Al-Kahtany, K.M., 2020. Petrological characteristics of the Neoproterozoic Ess ophiolite mantle section, Arabian Shield, Saudi Arabia: a mineral chemistry perspective. International Journal of Earth Sciences, 109, 239-251.

Gahlan, H.A., Azer, M.K., Al-Hashim, M.H., Osman, M.S., 2022. New insights and constraints on the late Neoproterozoic post-collisional mafic magmatism in the Arabian Shield, Saudi Arabia. Lithos, 436-437 (January 2023), 106989.

Gamal El Dien, H.M., Hamdy, M.M., Abu El Ela, A., Abu Alam, T., Hassan, A., Kil, Y., Mizukami, T., Soda, Y., 2016. Neoproterozoic serpentinites from the Eastern Desert of Egypt: Insights into Neoproterozoic mantle geodynamics and processes beneath the Arabian–Nubian Shield. Precambrian Research, 286, 213-233. DOI: 10.1016/j.precamres.2016.10.006

Gervilla, F., Padrón-Navarta, J.A., Kerestedjian, T., Sergeeva, I., González-Jiménez, J.M., Fanlo, I., 2012. Formation of ferrian chromite in podiform chromitites from the Golyamo Kamenyane serpentinite, Eastern Rhodopes, SE Bulgaria: a two-stage process. Contributions to Mineralogy and Petrology, 164(4), 643-657.

Ghoneim, M.F., 1989. Mineral chemistry of some gabbroic rocks of the central Eastern Desert, Egypt. Journal of African Earth Sciences, 9, 289-295.

Girardeau, J., Mevel, C., 1982. Amphibolized sheared gabbros from ophiolites as indicators of the evolution of the oceanic crust: Bay of islands, Newfoundland. Earth and Planetary Science Letters, 61, 151-165.

Gruau, G., Bernard-Griffiths, J., Lécuyer, C., 1998. The origin of U-shaped rare earth patterns in ophiolite peridotites: assessing the role of secondary alteration and melt/rock reaction. Geochimica et Cosmochimica Acta, 62(21/22), 3545-3560.

Hart, S.R., Zindler, A., 1986. In search of a bulk-Earth composition. Chemical Geology, 57, 247-267.

Hassan, S.F., Sadek, M.F., 2017. Geological mapping and spectral based classification of basement rocks using remote sensing data analysis: The Korbiai-Gerf nappe complex, South Eastern Desert, Egypt. Journal of African Earth Sciences, 134, 404-418.

Hattori, K.H., Guillot, S., 2007. Geochemical character of serpentinites associated with high- to ultrahigh-pressure metamorphic rocks in the Alps, Cuba, and the Himalayas: recycling of elements in subduction zones. Geochemistry, Geophysics, Geosystems, 8(9). Q09010. DOI: http://dx.doi.org/10.1029/2007GC001594

Hellebrand, E., Snow, J.E., Dick, H.J.B., Hofmann, A.W., 2001. Coupled major and trace elements as indicators of the extent of melting in mid-ocean-ridge peridotites. Nature, 410, 677-681.

Helmy, H.M., 2005. Melonite group minerals and other tellurides from three Cu-Ni-PGE prospects, Eastern Desert, Egypt. Ore Geology Reviews, 26, 305-324.

Helmy, H.M., El Mahallawi, M.M., 2003. Gabbro Akarem mafic-ultramafic complex, Eastern Desert, Egypt: a Late Precambrian analogue of Alaskan-type complex. Mineralogy and Petrology, 77, 85-108.

Helmy, H.M., Yoshikawa, M., Shibata, T., Arai, S., Kagami, H., 2015. Sm-Nd dating and petrology of Abu Hamamid intrusion, Eastern Desert, Egypt: a case of Neoproterozoic Alaskan-type complex in a backarc setting. Precambrian Research, 258, 234-246.

Hey, M.H., 1954. A new review of the chlorites. Mineralogical Magazine, 30, 277-292.

Ishii, T., Robinson, P.T., Maekawa, H., Fiske, R., 1992. Petrological studies of peridotites from diapiric serpentinite seamounts in the Izu-Ogasawara-Mariana forearc, leg 125. In: Fryer, P., Pearce, J.A., Stokking, L.B. (eds.). Proceedings of the Ocean Drilling Project, Leg 125. Scientific Results (College Station), 445-485.

Jagoutz, E., Palme, H., Baddenhausen, H., Blum, K., Cendales, M., Dreibus, G., Spettel, B., Lorenz, V., Wanke, H., 1979. The abundances of major, minor and trace elements in the earth's mantle as derived from primitive ultramafic nodules. Proceedings of Lunar Planetary Science Conference, 10, 2031-2050.

Jöns, N., Schenk, V., 2007. Relics of the Mozambique Ocean in the central Eastern African Orogen: evidence from the Vohibory Block of southern Madagascar. Journal of Metamorphic Geology, 26, 17-28.

JunBing, C., ZhiGang, Z., 2007. Metasomatism of the peridotites from southern Mariana fore-arc: Trace element characteristics of clinopyroxene and amphibole. Science in China Series D: Earth Sciences, 50, 1005-1012. DOI: 10.1007/s11430-007-0023-y

Kamenetsky, V.S., Crawford, A.J., Meffre, S., 2001. Factors controlling chemistry of magmatic spinel: An empirical study of associated olivine, Cr-spinel and melt inclusions from primitive rocks. Journal of Petrology, 42(4), 655-671. DOI: 10.1093/petrology/42.4.655

Kapsiotis, A., Grammatikopoulos, T.A., Tsikouras, B., Hatzipanagiotou, K., 2009. Chromian spinel composition and platinum-group element mineralogy of chromitites from the Milia area, Pindos ophiolite complex, Greece. The Canadian Mineralogist, 47(5), 1037-1056. DOI: 10.3749/canmin.47.5.1037

Kepezhinskas, P.K., Taylor, R.N., Tanaka, H., 1993. Geochemistry of plutonic spinels from the north Kamchatka arc: comparisons with spinels from other tectonic settings. Mineralogical Magazine, 57, 575-589.

Khalil, K.I., 2007. Chromite mineralization in ultramafic rocks of the Wadi Ghadir area, Eastern Desert, Egypt: mineralogical, microchemical and genetic study. Neues Jahrbcuh für Mineralogie - Abhandlungen, 183, 283-296.

Khalil, A.E.S., Azer, M.K., 2007. Supra-subduction affinity in the Neoproterozoic serpentinites in the Eastern Desert, Egypt: evidence from mineral composition. Journal of African Earth Sciences, 49, 136-152.

Khalil, A.E.S., Obeid, M.A., Azer, M.K., 2014. Serpentinized peridotites at the north part of Wadi Allaqi district (Egypt): Implications for the tectono-magmatic evolution of fore-arc crust. Acta Geologica Sinica, 88(5), 1421-1436.

Khedr, M.Z., Arai, S., 2012. Petrology and geochemistry of prograde deserpentinized peridotites from Happo-Óne, Japan: Evidence of element mobility during deserpentinization. Journal of Asian Earth Science, 43, 150-163. DOI: 10.1016/j.jseaes.2011.08.017

Khedr, M.Z., Arai, S., 2013. Origin of Neoproterozoic ophiolitic peridotites in south Eastern Desert, Egypt, constrained from primary mantle mineral chemistry. Mineralogy and Petrology, 107(5), 807-828.

Khedr, M.Z., Arai, S., 2017. Peridotite-chromitite complexes in the Eastern Desert of Egypt: Insight into Neoproterozoic sub-arc mantle processes. Gondwana Research, 52, 59-79. DOI: 10.1016/j.gr.2017.09.001

Kimball, K.L., Spear, F.S., Dick, H.J.B., 1985. High temperature alteration of abyssal ultramafics from the Islas Orcadas fracture zone, south Atlantic. Contributions to Mineralogy and Petrology, 91, 307-320. DOI: 10.1007/BF00374687

Kodolanyi, J., Pettke, T., Spandler, C., Kamber, B.S., Gmeling, K., 2012. Geochemistry of Ocean Floor and Fore-arc Serpentinites: Constraints on the Ultramafic Input to Subduction Zones. Journal of Petrology, 53(2), 235-270.

Le Bas, M.J., 1962. The role of aluminum in igneous clinopyroxenes with relation to their parentage. American Journal of Science, 260, 267-288. DOI: 10.2475/ajs.260.4.267

Leake, B.E., Woolley, A.R., Arps, C.E.S., Birch, W.D., Gilbert, M.C., Grice, J.D., Hawhorne, F.C., Kato, A., Kisch, H.J., Krivovichev, V.G., Linthout, K., Laird, J., Mandarino, J.A., Maresch, W.V., Nickel, E.H., Rock, N.M.S., Schumacher, J.C., Smith, D.C., Stephenson, N.C.N., Ungaretti, L., Whittaker, E.J.W., Youzhi, G., 1997. Nomenclature of amphiboles: Report of the subcommittee on amphiboles of the International Mineralogical Association, Commission on New Minerals and Mineral Names. American Mineralogist: Journal of Earth and Planetary Materials, 82, 1019-1037.

Martin, B., Fyfe, W.S., 1970. Some experimental and theoretical observations on the kinetics of hydration reactions with particular reference to serpentinization. Chemical Geology, 6, 185-202.

McDonough, W.F., Sun, S.S., 1995. The composition of the Earth. Chemical Geology, 120, 223-253.

Mellini, M., Rumori, C., Viti, C., 2005. Hydrothermally reset magmatic spinels in retrograde serpentinites: formation of "ferritchromit" rims and chlorite aureoles. Contributions to Mineralogy and Petrology, 149, 266-275.

Mével, C., 2003. Serpentinization of abyssal peridotites at mid-ocean ridges. Comptes Rendus Géoscience, 335, 825-852.

Michael, P.J., Bonatti, E., 1985. Peridotite composition from the North Atlantic; regional and tectonic variations and implications for partial melting. Earth and Planetary Science Letters, 73, 91-104.

Morimoto, N.F.J., Ferguson, A.K., Ginzburg, I.V., Ross, M., Seifert, F.A., Zussmaann, I., 1988. Nomenclature of pyroxene. Mineralogical Magazine, 52, 535-550. DOI: 10.1180/minmag.1988.052.367.15

Moussa, H.E., Azer, M.K., Abou El Maaty, M.A., Maurice, A.E., Yanni, N.N., Akarish, A.I., Elnazer, A.A., Elsagheer, M.A., 2021. Carbonation of Neoproterozoic mantle section and formation of gold-bearing listvenite in the Northern Nubian Shield. Lithos, 406-407, 106525.

Moussa, H.E., Mubarak, H.S., Azer, M.K., Surour, A.A., Asimow, P.D., Kabesh, M.M., 2022. Multistage petrogenetic evolution of Neoproterozoic serpentinized ultramafic rocks and podiform chromitites at Hagar Dungash, Eastern Desert of Egypt. Precambrian Research, 369, 106507.

Murata, K., Maekawa, H., Yokose, H., Yamamoto, K., Fujioka, K., Ishii, T., Chiba, H., Wada, Y., 2009. Significance of serpentinization of wedge mantle peridotites beneath Mariana forearc, western Pacific. Geosphere, 5, 90-104. DOI: 10.1130/GES00213.1

Müntener, O., Kelemen, P., Grove, T.L., 2001. The role of H2O during crystallization of primitive arc magmas under uppermost mantle conditions and genesis of igneous pyroxenites: an experimental study. Contributions to Mineralogy and Petrology, 141, 643-658.

Niu, Y., 2004. Bulk-rock major and trace element compositions of abyssal peridotites: implications for mantle melting, melt extraction and post-melting processes beneath mid-ocean ridges. Journal of Petrology, 45(12), 2423-2458.

Nozaka, T., 2010. A note on compositional variation of olivine and pyroxene in thermally metamorphosed ultramafic complexes from SW Japan. Okayama University, Earth Science Reports, 17(1), 1–5.

Obeid, M.A., Khalil, A.E.S., Azer, M.K., 2016. Mineralogy, geochemistry and geotectonic significance of the Neoproterozoic ophiolite of Wadi Arais area, south Eastern Desert, Egypt. International Geology Reviews, 58, 687-702. DOI: 10.1080/00206814.2015.1105727

Olivier, N., Boyet, M., 2006. Rare earth and trace elements of microbialites in Upper Jurassic coral- and sponge-microbialite reefs. Chemical Geology, 230, 105-123.

Ozawa, K., 1994. Melting and melt segregation in the mantle wedge above a subduction zone; evidence from the chromite-bearing peridotites of the Miyamori ophiolite complex, northeastern Japan. Journal of Petrology, 35, 647-678.

Parkinson, I.J., Arculus, R.J., 1999. The redox state of subduction zone: insights from arc peridotites. Chemical Geology, 160, 409-423.

Parkinson, I.J., Pearce, J.A., 1998. Peridotites from the Izu–Bonin–Mariana fore-arc (ODP Leg125): evidence for mantle melting and melt-mantle interaction in a supra-subduction zone setting. Journal of Petrology, 39, 1577-1618.

Paulick, H., Bach, W., Godard, M., De Hoog, J.C.M., Suhr, G., Harvey, J., 2006. Geochemistry of abyssal peridotites (Mid-Atlantic Ridge, 15°20′N, ODP Leg 209): implications for fluid/rock interaction in slow spreading environments. Chemical Geology, 234, 179-210.

Peacock, S.M., 1987. Serpentinization and infiltration metasomatism in the trinity peridotite, Klamath province, northern California: Implications for subduction zones. Contributions to Mineralogy and Petrology, 95, 55-70. DOI: 10.1007/BF00518030

Pearce, J.A., Barker, P.F., Edwards, S.J., Parkinson, I.J., Leat, P.T., 2000. Geochemistry and tectonic significance of peridotites from the south sandwich arc-basin system, South Atlantic. Contributions to Mineralogy and Petrology, 139, 36–53.

Pfeifer, H.-R., 1979. Fluid-Gestein-Interaktion in metamorphen Ultramafititen der Zentralalpen. Dissertatioen, ETH-Zürich. DOI: https://doi.org/10.3929/ethz-a-000185051

Python, M., Ceuleneer, G., Arai, S., 2008. Chromian spinels in mafic–ultramafic mantle dykes: Evidence for a two-stage melt production during the evolution of the Oman ophiolite. Lithos, 106, 137-154.

Roberts, S., 1992. Influence of partial melting regime on the formation of ophiolitic chromite. In: Parson, L.M., Murton, B.J., Browning, P. (eds.). Ophiolites and their Modern Oceanic Analogues. Geological Society, 6 (Special Publication), 203-217.

Sack, R.O., Ghiorso, M.S., 1991. Chromian spinels as petrogenetic indicators: thermodynamic and petrological applications. American Mineralogist, 76, 827-847.

Salters, V.J.M., Stracke, A., 2004. Composition of the depleted mantle. Geochemestry, Geophysics, Geosystems, 5(5), Q05B07. DOI: 10.1029/2003GC0005 97

Sedki, T., Ali, S., Mohamed, H.A., 2019. Geochemistry dataset of the Sol Hamed Neoproterozoic ophiolitic serpentinites, southern Eastern Desert, Egypt. Data in brief, 25, 104393. DOI: 10.1016/j.dib.2019.104393

Shackleton, R.M., 1994. Review of late Proterozoic sutures, ophiolitic mélanges and tectonics of eastern Egypt and North Sudan. Geologische Rundschau, 83, 537-546.

Sharma, M., Wasserburg, G.J., 1996. The neodymium isotopic compositions and rare earth patterns in highly depleted ultramafic rocks. Geochimica et Cosmochimica Acta, 60, 4537-4550.

Snow, J.E., Dick, H.J.B., 1995. Pervasive magnesium loss by marine weathering of peridotite. Geochimica et Cosmochimica Acta, 59, 4219-4235.

Stern, R.J., Fouch, M.J., Klemperer, S., 2003. An overview of the Izu-Bonin-Mariana Subduction Factory. In: Eiler, J., Hirschmann, M. (eds.). Inside the subduction factory. American Geophysical Union, Geophysical monograph, 138, 175-222.

Stern, R.J., Johnson, P.J., Kröner, A., Yibas, B., 2004. Neoproterozoic ophiolites of the Arabian–Nubian Shield. In: Kusky, T. (ed.). Precambrian Ophiolites. Elsevier, 13, 95–128.

Stevens, R.E., 1944, Composition of some Cr-spinels of the western hemisphere: American Mineralogist, 29(1-2), 1-34.

Suita, M., Strieder, A., 1996. Cr-spinels from Brazilian mafic–ultramafic complexes: metamorphic modifications. International Geology Review, 38(3), 245–267.

Sun, S.-S., Nesbitt, R.W., 1978. Geochemical irregularities and genetic significance of ophiolitic basalts. Geology, 6, 689-693.

Sun, S.S., McDonough, W.F., 1989. Chemical and systematic of Ocean basalts: implications for mantle composition and processes. In: Saunders, A.D., Norry, M.J. (eds.). Magmatism in Ocean Basins. London, The Geological Society, 42 (Special Publications), 42, 313-345.

Surour, A.A., 2017. Chemistry of serpentine "polymorphs" in the Pan-African serpentinites from the Eastern Desert of Egypt, with an emphasis on the effect of superimposed thermal metamorphism. Mineralogy and Petrology, 111, 99-119.

Takahashi, E., 1987, Origin of basaltic magmas–Implications from peridotite melting experiments and an olivine fractionation model. Bulletin of the Volcanological Society of Japan, 30, 17-40.

Whattam, S.A., Stern, R.J., 2011. The 'subduction initiation rule': a key for linking ophiolites, intra-oceanic forearcs and subduction initiation. Contributions to Mineralogy and Petrology, 162, 1031-1045.

Yang, S.-H., Zhou, M.-F., 2009. Geochemistry of the ~430-Ma Jingbulake mafic–ultramafic intrusion in Western Xinjiang, NM China: implications for subduction related magmatism in the South Tianshan orogenic belt. Lithos, 113, 259-273.

Zimmer, M., Kröner, A., Jochum, K.P., Reischmann, T., Todt, W., 1995. The Gabal Gerf complex: a Precambrian N-MORB ophiolite in the Nubian Shield, NE Africa. Chemical Geology, 123, 29-51.

Manuscript received March 2022;
revision accepted May 2023;
published Online July 2023.

APPENDIX

TABLE I. Electron probe microanalyses standards

	SiO_2	TiO_2	Al_2O_3	Cr_2O_3	FeO	MnO	MgO	CaO	Na_2O	K_2O	P_2O_5	ZrO_2	HfO_2	SrO	BaO
Shankland forsterite	42.706						57.294								
RDS fayalite	29.487				70.514										
RDS Mn-olivine	29.752					70.248									
Amelia albite	68.729		19.43						11.75	0.09					
Asbestos microcline	64.001		18.37		0.02		0.02	0.18	0.181	16.31					0.1
Anorthite synthetic	42.96		36.65		0.012		0.046	20.34	0.059	0.011				0.043	0.012
TiO_2 synthetic		100													
Cr_2O_3 synthetic				100											
Durango fluorapatite	0.351		0.07		0.05			54.02	0.187		40.881	0.014		0.056	
Pacoima zircon	32.779											64.16	2.59		
	Fe	S													
Pyrite synthetic	46.549	53.451													

TABLE I. Continued

	CO_2	SO_3	F	Cl	As_2O_3	La_2O_3	Ce_2O_3	Pr_2O_3	Nd_2O_3	Sm_2O_3	Gd_2O_3	Dy_2O_3	ThO_2	
Shankland forsterite														
RDS fayalite														
RDS Mn-olivine														
Amelia albite														
Asbestos microcline														
Anorthite synthetic														
TiO_2 synthetic														
Cr_2O_3 synthetic														
Durango fluorapatite	0.051	0.37	3.53	0.373	0.092	0.468	0.591	0.06	0.18	0.027	0.029	0.017		0.035
Pacoima zircon														
Pyrite synthetic														

TABLE II. Electron probe microanalyses of chromite in the studied mantle rocks

Area									Kadaboura									
Rock type									Serpentinites									
Sample No.									KD217									
Spot No.	#21C	#22C	#23R	#33C	#34C	#45C	#46C	#47R	#57C	#77C	#78C	#79R	#83C	#96C	#97R	#98R	#108C	#114C	#115C
Cr_2O_3	53.45	44.43	5.27	50.30	40.58	51.96	52.34	39.22	44.42	52.30	42.40	1.51	50.74	53.35	37.67	12.06	51.20	53.70	52.45
Al_2O_3	14.88	20.42	0.07	16.75	30.31	18.51	18.19	1.70	19.94	14.90	20.54	0.02	16.12	12.50	0.85	0.08	15.74	11.13	15.29
TiO_2	0.00	0.36	0.01	0.02	0.08	0.01	0.02	0.10	0.17	0.02	0.05	0.02	0.21	0.16	0.15	0.02	0.14	0.07	0.00
FeO^{total}	20.47	18.54	87.97	24.07	13.19	14.71	16.06	48.73	24.46	20.67	26.41	90.44	20.23	27.51	50.77	81.26	19.53	28.39	20.57
MgO	10.82	13.74	0.77	7.39	15.61	13.35	12.19	5.16	9.21	11.01	8.92	0.83	12.09	4.95	4.23	0.58	11.92	4.07	11.16
MnO	0.21	0.40	0.07	0.32	0.07	0.13	0.14	1.32	0.41	0.16	0.42	0.28	0.37	0.40	1.44	0.39	0.55	0.43	0.15
NiO	0.08	0.07	0.43	0.03	0.15	0.06	0.03	0.32	0.07	0.07	0.08	0.79	0.08	0.02	0.18	0.48	0.15	0.03	0.09
Total	99.92	97.96	94.58	98.87	99.99	98.73	98.97	96.55	98.67	99.13	98.82	93.88	99.84	98.89	95.29	94.87	99.23	97.83	99.71
Structural formula based on 32 oxygen atoms																			
Cr	10.892	8.808	1.261	10.511	7.533	10.368	10.520	8.989	9.046	10.712	8.611	0.362	10.196	11.556	8.836	2.891	10.373	11.895	10.661
Al	4.522	6.038	0.025	5.222	8.390	5.507	5.453	0.581	6.056	4.551	6.220	0.005	4.831	4.039	0.298	0.029	4.756	3.676	4.636
Ti	0.001	0.067	0.001	0.004	0.014	0.002	0.004	0.022	0.032	0.003	0.009	0.003	0.040	0.032	0.033	0.005	0.028	0.016	0.000
Fe^{3+}	0.580	1.004	11.330	0.258	0.049	0.120	0.018	5.748	0.823	0.722	1.130	11.811	0.881	0.338	6.078	10.401	0.805	0.395	0.695
Fe^{2+}	3.839	2.902	13.524	5.064	2.542	2.984	3.395	6.641	4.456	3.764	4.565	14.062	3.432	5.969	7.165	12.334	3.390	6.262	3.735
Mg	4.157	5.136	0.348	2.911	5.463	5.023	4.618	2.232	3.534	4.250	3.416	0.376	4.580	2.020	1.870	0.260	4.551	1.701	4.275
Mn	0.000	0.047	0.012	0.025	-0.019	-0.017	-0.015	0.284	0.050	-0.010	0.054	0.071	0.037	0.043	0.323	0.088	0.076	0.051	-0.012
Ni	0.016	0.015	0.104	0.006	0.029	0.013	0.006	0.076	0.014	0.015	0.016	0.194	0.016	0.005	0.044	0.117	0.031	0.008	0.018
Total	24.01	24.02	26.60	24.00	24.00	24.00	24.00	24.57	24.01	24.01	24.02	26.88	24.01	24.00	24.65	26.12	24.01	24.00	24.01
Cr#	71	59	98	67	47	65	66	94	60	70	58	99	68	74	97	99	69	76	70
Mg#	52	64	3	37	68	63	58	25	44	53	43	3	57	25	21	2	57	21	53

Cr#=100×Cr/(Cr+Al)
Mg#=100×Mg/(Mg+Fe^{2+})
C: unaltered core
R: altered rim

TABLE II. Continued

Area	Madara																							
Rock type	Serpentinites																							
Sample No.	KK37b																							
Spot No.	#8C	#17C	#18C	#19R	#30C	#51C	#52C	#57R	#76C	#86C	#87R	#88R	#94C	#108C	#109C	#110R	#121C	#122C	#123R	#135C	#136C	#137R	#153C	#154C	#155R
Cr_2O_3	46.24	54.56	52.35	17.34	47.85	54.49	47.02	3.87	44.40	52.11	37.15	6.17	44.17	52.75	44.47	7.61	53.55	45.11	5.08	53.21	48.59	1.48	51.52	47.93	12.36
Al_2O_3	20.12	15.14	14.75	0.18	19.92	11.62	14.66	0.07	19.79	14.27	0.70	0.02	19.38	15.17	20.34	0.05	15.30	16.80	0.04	14.97	14.34	0.04	18.04	14.17	1.82
TiO_2	0.10	0.03	0.00	0.01	0.10	0.05	0.36	0.00	0.18	0.04	0.15	0.03	0.19	0.01	0.36	0.00	0.02	0.36	0.01	0.03	0.27	0.01	0.00	0.29	0.03
FeO^{total}	20.45	19.58	21.19	73.92	21.22	27.09	23.16	88.38	24.96	25.23	51.79	85.50	25.53	21.29	18.79	83.18	19.19	22.27	86.26	24.22	23.57	90.48	15.85	23.54	69.40
MgO	12.48	10.48	10.70	2.34	10.27	4.65	11.46	0.59	9.50	6.05	3.89	0.97	9.45	10.96	14.07	1.44	10.49	11.86	1.06	6.98	10.72	1.36	12.46	10.61	6.95
MnO	0.35	0.16	0.17	0.93	0.30	0.38	1.08	0.23	0.38	0.35	1.81	0.37	0.39	0.20	0.50	0.24	0.14	1.00	0.23	0.33	0.77	0.05	0.14	0.85	0.37
NiO	0.08	0.05	0.08	0.53	0.06	0.02	0.05	0.47	0.08	0.00	0.13	0.77	0.06	0.09	0.13	0.68	0.09	0.05	0.92	0.03	0.05	0.37	0.04	0.06	0.37
Total	99.82	100.00	99.24	95.26	99.72	98.31	97.78	93.62	99.29	98.05	95.62	93.82	99.16	100.47	98.66	93.19	98.79	97.45	93.61	99.77	98.30	93.79	98.05	97.45	91.29
Structural formula based on 32 oxygen atoms																									
Cr	9.114	11.131	10.742	4.092	9.600	11.944	9.702	0.936	8.978	11.198	8.711	1.486	8.957	10.671	8.747	1.839	11.034	9.225	1.224	11.152	10.051	0.353	10.421	10.003	2.898
Al	5.915	4.608	4.513	0.064	5.959	3.799	4.511	0.026	5.968	4.574	0.245	0.008	5.862	4.575	5.967	0.016	4.702	5.125	0.016	4.680	4.422	0.014	5.442	4.411	0.638
Ti	0.018	0.006	0.000	0.002	0.018	0.011	0.071	0.000	0.034	0.007	0.033	0.006	0.037	0.002	0.068	0.001	0.004	0.069	0.002	0.006	0.053	0.003	0.000	0.057	0.006
Fe^{3+}	0.920	0.248	0.736	9.649	0.401	0.235	1.603	11.504	0.971	0.212	6.218	11.212	1.089	0.741	1.129	11.018	0.256	1.477	11.354	0.156	1.389	11.811	0.136	1.439	10.029
Fe^{2+}	3.359	3.978	3.871	10.589	4.105	6.046	3.493	13.796	4.383	5.524	7.306	13.111	4.406	3.822	2.801	12.683	3.929	3.376	13.259	5.215	3.799	13.989	3.256	3.791	9.141
Mg	4.636	4.033	4.137	1.043	3.884	1.923	4.456	0.269	3.622	2.452	1.718	0.440	3.611	4.181	5.215	0.658	4.074	4.574	0.483	2.758	4.179	0.612	4.751	4.174	3.072
Mn	0.034	-0.013	-0.008	0.219	0.022	0.039	0.196	0.057	0.044	0.033	0.417	0.088	0.045	-0.002	0.067	0.054	-0.016	0.180	0.053	0.027	0.127	0.012	-0.015	0.147	0.079
Ni	0.017	0.010	0.017	0.127	0.013	0.005	0.010	0.115	0.015	0.000	0.031	0.189	0.012	0.018	0.026	0.167	0.019	0.010	0.227	0.007	0.010	0.090	0.009	0.012	0.088
Total	24.01	24.00	24.01	25.78	24.00	24.00	24.04	26.70	24.01	24.00	24.68	26.54	24.02	24.01	24.02	26.43	24.00	24.03	26.62	24.00	24.03	26.88	24.00	24.03	25.95
Cr#	61	71	70	98	62	76	68	97	60	71	97	99	60	70	59	99	70	64	99	70	69	96	66	69	82
Mg#	58	50	52	9	49	24	56	2	45	31	19	3	45	52	65	5	51	58	4	35	52	4	59	52	25

Cr#=100×Cr/(Cr+Al)
Mg#=100×Mg/(Mg+Fe^{2+})
C: unaltered core
R: altered rim

TABLE III. Electron probe microanalyses of olivine in the studied mantle rocks

Rock type	Serpentinites														
Area	Kadaboura						Madara								
Sample No.	KD217						KK37b								
Spot No.	#18	#29	#37	#54	#64	#101	#15	#37	#47	#66	#84	#106	#133	#151	#161
SiO_2	41.15	41.06	41.31	40.46	40.99	40.91	41.21	41.24	40.65	41.00	40.64	40.67	41.31	40.46	41.08
TiO_2	0.01	0.00	0.01	0.01	0.01	0.01	0.00	0.01	0.00	0.00	0.01	0.01	0.00	0.00	0.00
Al_2O_3	0.00	0.00	0.02	0.00	0.01	0.00	0.02	0.01	0.02	0.01	0.00	0.00	0.01	0.07	0.09
Cr_2O_3	0.01	0.01	0.05	0.01	0.00	0.02	0.01	0.02	0.02	0.02	0.02	0.01	0.04	0.01	0.01
FeO	5.99	7.76	8.41	8.77	8.98	7.17	8.19	8.05	8.47	8.28	7.20	8.42	8.51	8.26	7.48
MnO	0.30	0.13	0.12	0.14	0.12	0.14	0.12	0.13	0.15	0.12	0.15	0.14	0.11	0.13	0.14
MgO	51.10	49.10	49.18	50.29	48.80	51.58	49.91	50.18	50.38	48.95	51.76	50.13	49.26	50.82	50.54
NiO	0.53	0.45	0.43	0.31	0.45	0.53	0.58	0.40	0.32	0.41	0.44	0.37	0.39	0.33	0.47
CaO	0.03	0.06	0.04	0.01	0.04	0.06	0.05	0.05	0.09	0.07	0.08	0.04	0.02	0.05	0.05
Total	99.13	98.61	99.57	100.01	99.40	100.43	100.10	100.09	100.10	98.88	100.32	99.81	99.68	100.14	99.87
Structural formula based on 4 oxygen atoms															
Si	1.003	1.012	1.011	0.989	1.007	0.990	1.003	1.003	0.992	1.010	0.985	0.995	1.010	0.986	0.999
Ti	0.000	0.000	0.000	0.000	0.000	0.000	0.000	0.000	0.000	0.000	0.000	0.000	0.000	0.000	0.000
Al	0.000	0.000	0.001	0.000	0.000	0.000	0.001	0.000	0.001	0.000	0.000	0.000	0.000	0.002	0.002
Cr	0.000	0.000	0.001	0.000	0.000	0.000	0.000	0.000	0.000	0.000	0.000	0.000	0.001	0.000	0.000
Fe^{2+}	0.122	0.160	0.172	0.179	0.185	0.145	0.167	0.164	0.173	0.171	0.146	0.172	0.174	0.168	0.152
Mn	0.006	0.003	0.003	0.003	0.002	0.003	0.003	0.003	0.003	0.003	0.003	0.003	0.002	0.003	0.003
Mg	1.856	1.804	1.794	1.833	1.788	1.861	1.811	1.819	1.833	1.798	1.871	1.828	1.795	1.847	1.833
Ni	0.010	0.009	0.009	0.006	0.009	0.010	0.011	0.008	0.006	0.008	0.009	0.007	0.008	0.007	0.009
Ca	0.001	0.002	0.001	0.000	0.001	0.002	0.001	0.001	0.002	0.002	0.002	0.001	0.001	0.001	0.001
Total	3.00	2.99	2.99	3.01	2.99	3.01	3.00	3.00	3.01	2.99	3.02	3.01	2.99	3.01	3.00
Fo	94	92	91	91	91	93	92	92	91	91	93	91	91	92	92
Fa	6	8	9	9	9	7	8	8	9	9	7	9	9	8	8

Fo=100×Mg/(Mg+Fe^{2+})
Fa=100×Fe^{2+}/(Mg+Fe^{2+})

TABLE IV. Electron probe microanalyses of pyroxene in the studied mantle rocks

Rock type	Sepentinites															
Area	Kadaboura							Madara								
Sample No.	KD217							KK37b								
Mineral	Clinopyroxene			Orthopyroxene				Clinopyroxene		Orthopyroxene						
Spot No.	#7	#42	#62	#67	#81	#93	#111	#70	#140	#5	#23	#41	#61	#92	#113	#130
SiO_2	52.48	55.04	52.69	56.56	57.21	56.75	57.11	53.90	54.72	57.13	57.11	57.35	56.88	56.89	57.16	56.88
TiO_2	0.15	0.09	0.15	0.02	0.00	0.02	0.01	0.09	0.04	0.00	0.01	0.01	0.00	0.00	0.01	0.00
Al_2O_3	2.09	1.29	2.10	1.44	1.35	1.40	1.38	1.29	0.63	1.53	1.52	2.05	0.90	1.54	1.48	1.40
Cr_2O_3	0.39	0.39	0.42	0.52	0.54	0.47	0.64	0.41	0.30	0.80	0.80	0.45	0.77	0.77	0.80	0.73
FeO	4.16	1.68	4.15	5.59	5.13	5.61	4.94	3.01	2.16	5.16	5.29	4.47	5.29	4.98	5.30	5.40
MnO	0.16	0.10	0.16	0.11	0.12	0.10	0.12	0.11	0.12	0.13	0.11	0.13	0.13	0.13	0.12	0.11
MgO	16.30	17.11	15.50	34.59	34.09	34.16	34.61	17.54	18.10	33.91	34.07	33.98	34.40	33.92	34.06	33.60
CaO	23.80	24.27	24.23	0.58	1.14	0.62	0.88	23.80	23.91	1.01	0.99	1.49	1.09	1.07	1.02	1.06
Na_2O	0.21	0.12	0.19	0.01	0.00	0.01	0.00	0.11	0.16	0.01	0.01	0.00	0.00	0.02	0.01	0.01
K_2O	0.01	0.01	0.00	0.00	0.00	0.00	0.00	0.01	0.00	0.00	0.00	0.00	0.00	0.01	0.00	0.01
Total	99.83	100.12	99.58	99.54	99.70	99.29	99.74	100.30	100.17	99.76	100.02	100.00	99.55	99.43	100.06	99.32
Structural formula based on 6 oxygen atoms																
Si	1.932	1.989	1.944	1.958	1.974	1.969	1.967	1.959	1.982	1.970	1.967	1.967	1.970	1.968	1.967	1.973
Ti	0.004	0.002	0.004	0.001	0.000	0.001	0.000	0.002	0.001	0.000	0.000	0.000	0.000	0.000	0.000	0.000
Al	0.091	0.055	0.091	0.059	0.055	0.057	0.056	0.055	0.027	0.062	0.062	0.083	0.037	0.063	0.060	0.057
Cr	0.011	0.011	0.012	0.014	0.015	0.013	0.017	0.012	0.008	0.022	0.022	0.012	0.021	0.021	0.022	0.020
Fe^{2+}	0.128	0.051	0.128	0.162	0.148	0.163	0.142	0.092	0.066	0.149	0.152	0.128	0.153	0.144	0.152	0.157
Mn	0.005	0.003	0.005	0.003	0.004	0.003	0.004	0.003	0.004	0.004	0.003	0.004	0.004	0.004	0.003	0.003
Mg	0.894	0.922	0.852	1.786	1.754	1.767	1.777	0.951	0.978	1.743	1.749	1.737	1.776	1.749	1.748	1.738
Ca	0.939	0.939	0.958	0.021	0.042	0.023	0.033	0.927	0.928	0.037	0.036	0.055	0.041	0.040	0.038	0.039
Na	0.015	0.008	0.013	0.001	0.000	0.001	0.000	0.008	0.012	0.001	0.000	0.000	0.000	0.001	0.001	0.000
K	0.000	0.000	0.000	0.000	0.000	0.000	0.000	0.000	0.000	0.000	0.000	0.000	0.000	0.000	0.000	0.000
Total	4.02	3.98	4.01	4.01	3.99	4.00	4.00	4.01	4.00	3.99	3.99	3.99	4.00	3.99	3.99	3.99
Mg#	93	89	89	92	91	91	92	94	95	90	91	91	92	91	91	90
En	0.47	0.47	0.44	0.91	0.89	0.90	0.91	0.49	0.50	0.89	0.89	0.89	0.90	0.89	0.89	0.88
Fs	0.04	0.06	0.06	0.08	0.09	0.09	0.08	0.03	0.03	0.09	0.09	0.09	0.08	0.09	0.09	0.10
Wo	0.49	0.48	0.50	0.01	0.02	0.01	0.02	0.48	0.47	0.02	0.02	0.03	0.02	0.02	0.02	0.02

Mg#=100×Mg/(Mg+Fe^{2+})

TABLE V. Electron probe microanalyses of amphibole in the studied mantle rocks

Rock type	Serpentinites															
Area	Kadaboura															
Sample No.	95/17															
Spot No.	93	94	95	96	99	102	103	104	110	111	112	114	115	117	118	119
SiO_2	46.59	45.01	42.29	44.39	37.10	43.36	40.72	43.03	45.23	43.77	41.96	42.13	45.87	44.55	44.56	44.33
TiO_2	0.00	0.00	0.00	0.00	0.00	0.00	0.00	0.00	0.00	0.00	0.00	0.00	0.00	0.00	0.00	0.00
Al_2O_3	0.04	0.00	0.00	0.00	9.64	0.25	0.00	0.13	0.00	0.00	0.00	0.00	0.06	0.00	0.00	0.00
Cr_2O_3	0.00	0.00	0.00	0.00	1.42	0.00	0.00	0.00	0.00	0.00	0.07	0.00	0.00	0.04	0.11	0.00
FeO	1.08	1.06	1.15	0.95	2.64	1.92	1.54	1.54	1.51	1.04	1.99	1.78	1.53	0.99	0.78	0.97
MnO	0.14	0.03	0.04	0.04	0.04	0.03	0.01	0.02	0.03	0.03	0.00	0.00	0.02	0.00	0.00	0.01
MgO	37.74	39.11	42.39	41.92	35.95	43.40	42.25	40.63	40.44	43.38	41.14	44.38	38.64	41.72	41.87	44.33
CaO	0.06	0.04	0.02	0.03	0.03	0.02	0.03	0.04	0.03	0.02	0.02	0.01	0.05	0.00	0.02	0.03
Na_2O	0.04	0.04	0.00	0.00	0.04	0.04	0.07	0.04	0.08	0.04	0.03	0.05	0.05	0.00	0.04	0.07
K_2O	0.01	0.00	0.00	0.00	0.00	0.00	0.02	0.00	0.00	0.00	0.01	0.00	0.01	0.00	0.00	0.00
NiO	0.27	0.20	0.13	0.13	0.24	0.18	0.27	0.14	0.05	0.01	0.16	0.10	0.17	0.21	0.11	0.16
Total	85.99	85.49	86.01	87.46	87.09	89.19	84.91	85.58	87.38	88.30	85.39	88.45	86.41	87.51	87.48	89.89
Structural formula on 7 (O) anhydrous basis																
Si	2.16	2.11	1.99	2.04	1.74	1.97	1.95	2.03	2.08	2.00	2.00	1.94	2.13	2.05	2.05	1.99
Ti	0.00	0.00	0.00	0.00	0.00	0.00	0.00	0.00	0.00	0.00	0.00	0.00	0.00	0.00	0.00	0.00
Al	0.00	0.00	0.00	0.00	0.53	0.01	0.00	0.01	0.00	0.00	0.00	0.00	0.00	0.00	0.00	0.00
Cr	0.00	0.00	0.00	0.00	0.05	0.00	0.00	0.00	0.00	0.00	0.00	0.00	0.00	0.00	0.00	0.00
Fe	0.04	0.04	0.05	0.04	0.10	0.07	0.06	0.06	0.06	0.04	0.08	0.07	0.06	0.04	0.03	0.04
Mn	0.01	0.00	0.00	0.00	0.00	0.00	0.00	0.00	0.00	0.00	0.00	0.00	0.00	0.00	0.00	0.00
Mg	2.61	2.73	2.97	2.87	2.52	2.95	3.02	2.86	2.77	2.96	2.92	3.05	2.67	2.86	2.87	2.97
Ca	0.00	0.00	0.00	0.00	0.00	0.00	0.00	0.00	0.00	0.00	0.00	0.00	0.00	0.00	0.00	0.00
Na	0.00	0.00	0.00	0.00	0.00	0.00	0.01	0.00	0.01	0.00	0.00	0.00	0.00	0.00	0.00	0.01
K	0.00	0.00	0.00	0.00	0.00	0.00	0.00	0.00	0.00	0.00	0.00	0.00	0.00	0.00	0.00	0.00
Ni	0.01	0.01	0.00	0.00	0.01	0.01	0.01	0.01	0.00	0.00	0.01	0.00	0.01	0.01	0.00	0.01
Total	4.84	4.89	5.01	4.96	4.97	5.02	5.05	4.97	4.92	5.00	5.01	5.06	4.87	4.95	4.95	5.01

TABLE VI. Electron probe microanalyses of serpentine in the studied mantle rocks

Rock type	Serpentinites															
Area	Kadaboura															
Sample No.	95/17															
Spot No.	93	94	95	96	99	102	103	104	110	111	112	114	115	117	118	119
SiO_2	46.59	45.01	42.29	44.39	37.10	43.36	40.72	43.03	45.23	43.77	41.96	42.13	45.87	44.55	44.56	44.33
TiO_2	0.00	0.00	0.00	0.00	0.00	0.00	0.00	0.00	0.00	0.00	0.00	0.00	0.00	0.00	0.00	0.00
Al_2O_3	0.04	0.00	0.00	0.00	9.64	0.25	0.00	0.13	0.00	0.00	0.00	0.00	0.06	0.00	0.00	0.00
Cr_2O_3	0.00	0.00	0.00	0.00	1.42	0.00	0.00	0.00	0.00	0.00	0.07	0.00	0.00	0.04	0.11	0.00
FeO	1.08	1.06	1.15	0.95	2.64	1.92	1.54	1.54	1.51	1.04	1.99	1.78	1.53	0.99	0.78	0.97
MnO	0.14	0.03	0.04	0.04	0.04	0.03	0.01	0.02	0.03	0.03	0.00	0.00	0.02	0.00	0.00	0.01
MgO	37.74	39.11	42.39	41.92	35.95	43.40	42.25	40.63	40.44	43.38	41.14	44.38	38.64	41.72	41.87	44.33
CaO	0.06	0.04	0.02	0.03	0.03	0.02	0.03	0.04	0.03	0.02	0.02	0.01	0.05	0.00	0.02	0.03
Na_2O	0.04	0.04	0.00	0.00	0.04	0.04	0.07	0.04	0.08	0.04	0.03	0.05	0.05	0.00	0.04	0.07
K_2O	0.01	0.00	0.00	0.00	0.00	0.00	0.02	0.00	0.00	0.00	0.01	0.00	0.01	0.00	0.00	0.00
NiO	0.27	0.20	0.13	0.13	0.24	0.18	0.27	0.14	0.05	0.01	0.16	0.10	0.17	0.21	0.11	0.16
Total	85.99	85.49	86.01	87.46	87.09	89.19	84.91	85.58	87.38	88.30	85.39	88.45	86.41	87.51	87.48	89.89
Structural formula on 7 (O) anhydrous basis																
Si	2.16	2.11	1.99	2.04	1.74	1.97	1.95	2.03	2.08	2.00	2.00	1.94	2.13	2.05	2.05	1.99
Ti	0.00	0.00	0.00	0.00	0.00	0.00	0.00	0.00	0.00	0.00	0.00	0.00	0.00	0.00	0.00	0.00
Al	0.00	0.00	0.00	0.00	0.53	0.01	0.00	0.01	0.00	0.00	0.00	0.00	0.00	0.00	0.00	0.00
Cr	0.00	0.00	0.00	0.00	0.05	0.00	0.00	0.00	0.00	0.00	0.00	0.00	0.00	0.00	0.00	0.00
Fe	0.04	0.04	0.05	0.04	0.10	0.07	0.06	0.06	0.06	0.04	0.08	0.07	0.06	0.04	0.03	0.04
Mn	0.01	0.00	0.00	0.00	0.00	0.00	0.00	0.00	0.00	0.00	0.00	0.00	0.00	0.00	0.00	0.00
Mg	2.61	2.73	2.97	2.87	2.52	2.95	3.02	2.86	2.77	2.96	2.92	3.05	2.67	2.86	2.87	2.97
Ca	0.00	0.00	0.00	0.00	0.00	0.00	0.00	0.00	0.00	0.00	0.00	0.00	0.00	0.00	0.00	0.00
Na	0.00	0.00	0.00	0.00	0.00	0.00	0.01	0.00	0.01	0.00	0.00	0.00	0.00	0.00	0.00	0.01
K	0.00	0.00	0.00	0.00	0.00	0.00	0.00	0.00	0.00	0.00	0.00	0.00	0.00	0.00	0.00	0.00
Ni	0.01	0.01	0.00	0.00	0.01	0.01	0.01	0.01	0.00	0.00	0.01	0.00	0.01	0.01	0.00	0.01
Total	4.84	4.89	5.01	4.96	4.97	5.02	5.05	4.97	4.92	5.00	5.01	5.06	4.87	4.95	4.95	5.01

TABLE VI. Continued

	Serpentinites																
	Kadaboura															KD217	
	95/17																
	124	125	126	128	130	132	133	134	136	137	138	142	143	146	149	#6	#16
SiO_2	46.94	41.74	44.43	44.06	41.76	40.15	41.39	42.97	44.61	43.31	44.08	43.44	38.83	48.50	47.15	43.85	43.56
TiO_2	0.00	0.00	0.00	0.00	0.00	0.00	0.00	0.00	0.00	0.00	0.00	0.00	0.00	0.00	0.00	0.00	0.00
Al_2O_3	0.00	0.00	0.00	0.00	0.00	0.00	0.00	0.00	0.00	0.00	0.00	0.00	5.07	0.10	0.17	0.24	0.16
Cr_2O_3	0.00	0.00	0.00	0.00	0.00	0.00	0.00	0.04	0.00	0.08	0.00	0.04	0.97	0.03	0.00	0.05	0.02
FeO	1.16	0.98	1.24	1.05	0.95	0.89	0.96	1.30	1.11	1.43	1.31	1.24	5.04	2.83	4.66	4.87	1.82
MnO	0.01	0.02	0.04	0.37	0.01	0.00	0.03	0.02	0.00	0.05	0.04	0.03	0.30	0.11	0.06	0.03	0.01
MgO	39.80	41.97	38.90	43.04	43.16	44.11	42.18	41.89	42.41	42.94	40.99	40.18	37.61	36.48	33.74	38.62	41.16
CaO	0.03	0.02	0.03	0.04	0.02	0.03	0.02	0.03	0.03	0.04	0.05	0.02	0.04	0.10	0.06	0.00	0.00
Na_2O	0.05	0.02	0.00	0.05	0.00	0.00	0.03	0.04	0.04	0.02	0.08	0.05	0.12	0.07	0.04	0.01	0.00
K_2O	0.00	0.00	0.00	0.01	0.00	0.00	0.00	0.00	0.00	0.00	0.00	0.00	0.02	0.01	0.00	0.00	0.00
NiO	0.14	0.12	0.14	0.22	0.11	0.11	0.10	0.08	0.10	0.07	0.12	0.02	0.12	0.27	0.11	0.13	0.12
Total	88.13	84.87	84.77	88.85	86.01	85.29	84.69	86.37	88.30	87.96	86.67	85.03	88.12	88.51	85.98	87.79	86.85
Structural formula on 7 (O) anhydrous basis																	
Si	2.13	1.99	2.10	2.01	1.96	1.91	1.98	2.01	2.03	1.99	2.05	2.05	1.83	2.20	2.21	2.05	2.03
Ti	0.00	0.00	0.00	0.00	0.00	0.00	0.00	0.00	0.00	0.00	0.00	0.00	0.00	0.00	0.00	0.00	0.00
Al	0.00	0.00	0.00	0.00	0.00	0.00	0.00	0.00	0.00	0.00	0.00	0.00	0.28	0.01	0.01	0.01	0.01
Cr	0.00	0.00	0.00	0.00	0.00	0.00	0.00	0.00	0.00	0.00	0.00	0.00	0.04	0.00	0.00	0.00	0.00
Fe	0.04	0.04	0.05	0.04	0.04	0.04	0.04	0.05	0.04	0.06	0.05	0.05	0.20	0.11	0.18	0.19	0.07
Mn	0.00	0.00	0.00	0.01	0.00	0.00	0.00	0.00	0.00	0.00	0.00	0.00	0.01	0.00	0.00	0.00	0.00
Mg	2.69	2.98	2.74	2.92	3.03	3.13	3.00	2.92	2.88	2.95	2.84	2.83	2.64	2.46	2.36	2.69	2.86
Ca	0.00	0.00	0.00	0.00	0.00	0.00	0.00	0.00	0.00	0.00	0.00	0.00	0.00	0.00	0.00	0.00	0.00
Na	0.00	0.00	0.00	0.00	0.00	0.00	0.00	0.00	0.00	0.00	0.01	0.00	0.01	0.01	0.00	0.00	0.00
K	0.00	0.00	0.00	0.00	0.00	0.00	0.00	0.00	0.00	0.00	0.00	0.00	0.00	0.00	0.00	0.00	0.00
Ni	0.01	0.00	0.01	0.01	0.00	0.00	0.00	0.00	0.00	0.00	0.00	0.00	0.00	0.01	0.00	0.00	0.00
Total	4.87	5.01	4.90	5.00	5.04	5.09	5.03	4.99	4.97	5.01	4.96	4.95	5.02	4.80	4.78	4.95	4.97

TABLE VI. Continued

	Serpentinites																
	Kadaboura							Madara									
	KD217							KK37b									
	#26	#41	#51	#60	#72	#89	#106	#1	#2	#14	#27	#29	#36	#49	#58	#72	#75
SiO_2	43.00	31.22	41.89	42.87	42.47	44.12	44.00	42.02	43.45	41.36	44.27	46.42	26.69	42.62	35.26	43.68	43.31
TiO_2	0.00	0.00	0.00	0.00	0.00	0.00	0.00	0.00	0.00	0.00	0.00	0.00	0.00	0.00	0.00	0.00	0.00
Al_2O_3	0.53	0.14	0.44	0.27	0.80	0.32	0.42	0.32	0.93	0.31	0.36	0.37	0.29	0.50	0.34	0.36	0.37
Cr_2O_3	0.04	0.26	0.40	0.16	0.30	0.07	0.21	0.04	0.55	0.37	0.11	0.14	0.09	0.18	0.19	0.17	0.10
FeO	3.66	28.40	4.93	4.24	4.40	3.04	3.98	6.14	4.33	6.36	4.09	4.20	40.02	5.56	20.83	3.97	4.60
MnO	0.03	0.03	0.07	0.08	0.07	0.01	0.04	0.18	0.03	0.21	0.04	0.10	0.05	0.12	0.03	0.03	0.03
MgO	37.88	27.83	37.25	37.77	36.85	38.93	38.05	35.69	37.64	36.38	38.12	35.68	23.16	36.00	29.65	36.89	37.71
CaO	0.01	0.01	0.04	0.04	0.03	0.00	0.00	0.02	0.00	0.02	0.00	1.90	0.00	0.02	0.00	0.00	0.00
Na_2O	0.00	0.01	0.00	0.00	0.00	0.00	0.00	0.01	0.00	0.01	0.00	0.01	0.01	0.00	0.01	0.00	0.00
K_2O	0.00	0.00	0.00	0.00	0.00	0.00	0.00	0.00	0.00	0.01	0.00	0.00	0.00	0.00	0.00	5.33	0.00
NiO	0.12	0.25	0.28	0.28	0.56	0.11	0.11	0.36	0.17	0.17	0.11	0.11	0.06	0.23	0.10	0.13	0.09
Total	85.26	88.14	85.29	85.70	85.49	86.60	86.81	84.79	87.10	85.19	87.10	88.92	90.37	85.22	86.42	90.55	86.22
Structural formula on 7 (O) anhydrous basis																	
Si	2.05	1.70	2.02	2.05	2.04	2.06	2.07	2.05	2.04	2.02	2.07	2.13	1.53	2.06	1.85	2.04	2.05
Ti	0.00	0.00	0.00	0.00	0.00	0.00	0.00	0.00	0.00	0.00	0.00	0.00	0.00	0.00	0.00	0.00	0.00
Al	0.03	0.01	0.02	0.02	0.05	0.02	0.02	0.02	0.05	0.02	0.02	0.02	0.02	0.03	0.02	0.02	0.02
Cr	0.00	0.01	0.02	0.01	0.01	0.00	0.01	0.00	0.02	0.01	0.00	0.01	0.00	0.01	0.01	0.01	0.00
Fe	0.15	1.29	0.20	0.17	0.18	0.12	0.16	0.25	0.17	0.26	0.16	0.16	1.92	0.22	0.92	0.15	0.18
Mn	0.00	0.00	0.00	0.00	0.00	0.00	0.00	0.01	0.00	0.01	0.00	0.00	0.00	0.00	0.00	0.00	0.00
Mg	2.70	2.26	2.68	2.69	2.64	2.72	2.66	2.60	2.63	2.64	2.66	2.44	1.98	2.59	2.32	2.57	2.67
Ca	0.00	0.00	0.00	0.00	0.00	0.00	0.00	0.00	0.00	0.00	0.00	0.09	0.00	0.00	0.00	0.00	0.00
Na	0.00	0.00	0.00	0.00	0.00	0.00	0.00	0.00	0.00	0.00	0.00	0.00	0.00	0.00	0.00	0.00	0.00
K	0.00	0.00	0.00	0.00	0.00	0.00	0.00	0.00	0.00	0.00	0.00	0.00	0.00	0.00	0.00	0.32	0.00
Ni	0.00	0.01	0.01	0.01	0.02	0.00	0.00	0.01	0.01	0.01	0.00	0.00	0.00	0.01	0.00	0.00	0.00
Total	4.93	5.29	4.96	4.94	4.93	4.93	4.92	4.94	4.92	4.97	4.92	4.86	5.46	4.92	5.13	5.11	4.93

TABLE VI. Continued

	Serpentinites							Pyroxenite				
							Madara					
			KK37b							A		
	#81	#96	#118	#120	#128	#145	#158	18	37	39	40	42
SiO_2	44.32	44.62	43.74	43.78	38.20	44.27	43.87	44.49	42.09	40.56	44.50	44.97
TiO_2	0.00	0.00	0.00	0.00	0.00	0.00	0.00	0.00	0.00	0.00	0.00	0.00
Al_2O_3	0.33	0.31	0.43	0.51	0.25	0.31	0.20	0.00	0.00	0.05	0.09	0.16
Cr_2O_3	0.08	0.14	0.22	0.12	0.03	0.07	0.02	0.00	0.00	0.00	0.00	0.04
FeO	3.58	3.58	4.22	4.03	13.49	3.25	2.82	1.13	1.69	1.51	1.97	2.10
MnO	0.03	0.02	0.05	0.04	0.03	0.03	0.04	0.00	0.00	0.00	0.00	0.00
MgO	38.10	38.47	37.74	37.50	35.38	38.00	39.81	38.14	40.53	41.97	39.73	38.49
CaO	0.00	0.00	0.00	0.00	0.00	0.00	0.00	0.10	0.07	0.06	0.03	0.02
Na_2O	0.00	0.01	0.00	0.00	0.01	0.01	0.00	0.12	0.22	0.14	0.02	0.00
K_2O	0.00	0.00	0.00	0.00	0.00	0.00	0.00	0.02	0.05	0.03	0.00	0.01
NiO	0.10	0.11	0.23	0.13	0.11	0.17	0.18	0.33	0.46	0.26	0.17	0.19
Total	86.55	87.26	86.64	86.11	87.48	86.10	86.95	84.33	85.11	84.57	86.51	85.99
Structural formula on 7 (O) anhydrous basis												
Si	2.08	2.08	2.06	2.07	1.90	2.08	2.05	2.11	2.01	1.95	2.07	2.10
Ti	0.00	0.00	0.00	0.00	0.00	0.00	0.00	0.00	0.00	0.00	0.00	0.00
Al	0.02	0.02	0.02	0.03	0.01	0.02	0.01	0.00	0.00	0.00	0.00	0.01
Cr	0.00	0.01	0.01	0.00	0.00	0.00	0.00	0.00	0.00	0.00	0.00	0.00
Fe	0.14	0.14	0.17	0.16	0.56	0.13	0.11	0.04	0.07	0.06	0.08	0.08
Mn	0.00	0.00	0.00	0.00	0.00	0.00	0.00	0.00	0.00	0.00	0.00	0.00
Mg	2.66	2.67	2.65	2.64	2.62	2.67	2.77	2.70	2.88	3.01	2.76	2.69
Ca	0.00	0.00	0.00	0.00	0.00	0.00	0.00	0.01	0.00	0.00	0.00	0.00
Na	0.00	0.00	0.00	0.00	0.00	0.00	0.00	0.01	0.02	0.01	0.00	0.00
K	0.00	0.00	0.00	0.00	0.00	0.00	0.00	0.00	0.00	0.00	0.00	0.00
Ni	0.00	0.00	0.01	0.00	0.00	0.01	0.01	0.01	0.02	0.01	0.01	0.01
Total	4.91	4.91	4.92	4.91	5.10	4.91	4.95	4.89	5.00	5.05	4.92	4.89

TABLE VII. Electron probe microanalyses of chlorite in the studied mantle rocks

Rock type	Serpentinites													
Area	Kadaboura					Madara								
Sample No.	KD217					KK37b								
Spot No.	#12	#24	#74	#86	#118	#13	#31	#54	#69	#79	#95	#117	#129	#146
SiO_2	26.63	29.30	28.92	30.93	31.25	29.91	27.73	29.86	29.57	30.72	29.57	30.76	27.04	27.50
TiO_2	0.02	0.01	0.11	0.01	0.01	0.02	0.16	0.02	0.03	0.02	0.07	0.01	0.02	0.03
Al_2O_3	19.72	17.82	18.38	16.37	16.42	17.98	18.47	16.92	18.32	16.34	17.87	16.41	19.98	19.85
FeO	11.63	8.69	14.50	7.96	5.32	6.06	17.16	8.39	8.63	5.10	9.59	8.33	11.51	11.39
MnO	0.08	0.03	0.04	0.02	0.00	0.02	0.06	0.01	0.03	0.01	0.02	0.01	0.08	0.09
MgO	22.80	27.15	22.53	27.93	29.69	29.11	19.89	27.56	27.00	30.26	26.22	27.55	21.97	21.86
CaO	0.01	0.02	0.08	0.03	0.06	0.01	0.16	0.04	0.04	0.02	0.06	0.02	0.02	0.03
Na_2O	0.01	0.01	0.03	0.02	0.01	0.01	0.02	0.02	0.01	0.02	0.02	0.01	0.01	0.02
K_2O	0.02	0.04	0.04	0.01	0.01	0.01	0.06	0.02	0.02	0.04	0.02	0.02	0.02	0.09
Cr_2O_3	3.54	1.06	1.41	1.56	1.00	0.85	1.66	1.38	1.31	1.77	1.10	1.17	3.68	3.20
NiO	0.73	0.86	0.48	0.80	0.72	1.26	0.67	0.89	0.55	0.78	0.69	1.00	0.64	0.84
Total	85.20	84.99	86.53	85.62	84.51	85.23	86.04	85.11	85.50	85.09	85.24	85.29	84.95	84.89
Structural formula based on 28 oxygen atoms														
Si	5.439	5.858	5.830	6.097	6.141	5.886	5.727	5.956	5.854	6.027	5.904	6.100	5.511	5.596
Al^{iv}	2.561	2.142	2.170	1.903	1.859	2.114	2.273	2.044	2.146	1.973	2.096	1.900	2.489	2.404
Al^{vi}	2.198	2.063	2.212	1.911	1.954	2.060	2.238	1.939	2.138	1.810	2.119	1.946	2.331	2.380
Ti	0.003	0.002	0.017	0.002	0.002	0.003	0.025	0.003	0.005	0.003	0.011	0.002	0.003	0.004
Cr	0.571	0.168	0.225	0.243	0.155	0.132	0.271	0.217	0.204	0.274	0.174	0.184	0.593	0.514
Fe^{3+}	0.115	0.046	0.157	0.139	0.140	0.045	0.148	0.061	0.110	0.058	0.116	0.127	0.241	0.263
Fe^{2+}	1.872	1.407	2.287	1.173	0.735	0.953	2.816	1.338	1.318	0.780	1.485	1.254	1.720	1.675
Mn	0.015	0.004	0.008	0.004	0.001	0.003	0.010	0.002	0.006	0.002	0.004	0.002	0.014	0.015
Mg	6.944	8.092	6.770	8.207	8.697	8.539	6.124	8.194	7.970	8.849	7.804	8.145	6.675	6.631
Ni	0.120	0.138	0.077	0.126	0.114	0.199	0.112	0.143	0.087	0.124	0.111	0.159	0.105	0.138
Ca	0.003	0.004	0.017	0.006	0.013	0.002	0.035	0.008	0.008	0.004	0.012	0.004	0.004	0.007
Na	0.009	0.008	0.027	0.013	0.010	0.005	0.018	0.014	0.011	0.012	0.014	0.008	0.006	0.017
K	0.011	0.019	0.019	0.004	0.006	0.005	0.034	0.011	0.009	0.022	0.011	0.012	0.008	0.046
OH*	16.000	16.000	16.000	16.000	16.000	16.000	16.000	16.000	16.000	16.000	16.000	16.000	16.000	16.000
Total	35.86	35.95	35.82	35.83	35.83	35.95	35.83	35.93	35.87	35.94	35.86	35.84	35.70	35.69
Fe/Fe+Mg	0.22	0.15	0.27	0.14	0.09	0.10	0.33	0.15	0.15	0.09	0.17	0.14	0.23	0.23

TABLE VIII. Electron probe microanalyses of talc in the studied mantle rocks

Area	Kadaboura					Madara									
Rock type	Dunite					Serpentinites						Pyroxenite			
Sample No.	95/5				KD217	KK37b						A			
Spot No.	5'	6'	7'	8'	#103	#6	#26	#44	#100	#125	#142	23	30	35	43
SiO_2	52.92	52.06	55.10	62.17	61.29	62.11	62.03	61.10	62.02	61.39	61.60	52.87	56.65	69.93	66.06
TiO_2	0.00	0.00	0.00	0.00	0.02	0.01	0.01	0.01	0.01	0.01	0.01	0.00	0.00	0.00	0.00
Al_2O_3	0.03	0.14	0.11	0.16	0.25	0.11	0.13	0.25	0.26	0.20	0.12	0.00	0.07	0.00	0.07
Cr_2O_3	0.00	0.00	0.00	0.00	0.11	0.07	0.07	0.08	0.14	0.08	0.07	0.00	0.00	0.00	0.00
FeO	2.10	3.12	1.99	1.57	2.12	1.86	1.87	1.87	2.01	1.88	1.85	1.56	1.22	0.84	1.31
MnO	0.00	0.10	0.00	0.00	0.01	0.02	0.01	0.01	0.01	0.01	0.01	0.00	0.00	0.04	0.00
MgO	30.08	33.77	34.19	29.27	28.51	28.87	28.85	28.85	27.98	29.28	28.83	32.03	29.25	18.36	23.91
NiO	0.24	0.13	0.22	0.24	0.01	0.01	0.01	0.01	0.01	0.01	0.02	0.18	0.16	0.10	0.13
CaO	0.02	0.03	0.00	0.18	1.69	1.41	1.86	2.01	1.85	2.14	1.76	0.08	0.14	0.14	0.04
Na_2O	0.02	0.03	0.00	0.06	0.02	0.01	0.02	0.01	0.02	0.02	0.01	0.09	0.06	0.13	0.04
K_2O	0.00	0.00	0.00	0.01	0.04	0.03	0.03	0.04	0.04	0.04	0.03	0.03	0.02	0.03	0.01
Total	85.42	89.38	91.61	93.66	94.07	94.50	94.89	94.24	94.35	95.05	94.31	86.84	87.56	89.55	91.56
Structural formula on 11 (O) anhydrous basis															
Si	3.81	3.63	3.71	4.02	3.98	4.00	3.99	3.96	4.01	3.95	3.99	3.75	3.93	4.57	4.30
Ti	0.00	0.00	0.00	0.00	0.00	0.00	0.00	0.00	0.00	0.00	0.00	0.00	0.00	0.00	0.00
Al	0.00	0.01	0.01	0.01	0.02	0.01	0.01	0.02	0.02	0.01	0.01	0.00	0.01	0.00	0.01
Cr	0.00	0.00	0.00	0.00	0.01	0.00	0.00	0.00	0.01	0.00	0.00	0.00	0.00	0.00	0.00
Fe*	0.13	0.18	0.11	0.09	0.12	0.10	0.10	0.10	0.11	0.10	0.10	0.09	0.07	0.05	0.07
Mn	0.00	0.01	0.00	0.00	0.00	0.00	0.00	0.00	0.00	0.00	0.00	0.00	0.00	0.00	0.00
Mg	3.23	3.51	3.44	2.82	2.76	2.77	2.77	2.79	2.70	2.81	2.78	3.39	3.03	1.79	2.32
Ca	0.01	0.01	0.01	0.01	0.00	0.00	0.00	0.00	0.00	0.00	0.00	0.01	0.01	0.00	0.01
Na	0.00	0.00	0.00	0.03	0.23	0.19	0.26	0.28	0.26	0.30	0.24	0.01	0.02	0.02	0.01
K	0.00	0.00	0.00	0.01	0.00	0.00	0.00	0.00	0.00	0.00	0.00	0.01	0.01	0.02	0.00

TABLE IX. Electron probe microanalyses of carbonate in the studied mantle rocks

Rock type	Serpentinites												
Mineral	Calcite									Magnesite			
Area	Kadaboura							Madara		Kadaboura			Madara
Sample No.	A19			KD217				KK37b		A19	KD217		KK37b
Spot No.	86	87	106	#38	#56	#66	#92	#148	#157	130	#30	#120	#11
SiO_2	1.14	0.73	1.39	0.00	0.00	0.00	0.00	0.00	0.00	1.35	0.00	0.00	0.00
TiO_2	0.01	0.00	0.00	0.00	0.00	0.00	0.00	0.00	0.00	0.00	0.00	0.00	0.00
Al_2O_3	0.00	0.00	0.00	0.00	0.00	0.00	0.00	0.00	0.00	0.00	0.00	0.00	0.00
Cr_2O_3	0.00	0.00	0.00	0.00	0.00	0.00	0.00	0.00	0.00	0.01	0.00	0.00	0.00
FeO	0.73	0.82	0.89	0.20	0.18	0.37	0.25	0.19	0.26	0.82	8.78	2.56	2.45
MnO	1.28	1.68	2.29	0.10	0.07	0.07	0.08	0.07	0.11	1.65	0.35	0.27	0.40
MgO	2.86	3.25	2.67	0.97	1.37	0.39	0.48	1.42	1.54	43.08	42.11	43.42	42.95
CaO	50.29	49.04	47.95	54.87	55.21	55.11	55.21	55.67	55.50	0.17	0.13	0.23	0.20
Na_2O	0.10	0.10	0.08	0.00	0.00	0.00	0.00	0.00	0.00	0.00	0.00	0.00	0.00
K_2O	0.04	0.04	0.06	0.00	0.00	0.00	0.00	0.00	0.00	0.01	0.00	0.00	0.00
NiO	0.08	0.14	0.10	0.00	0.00	0.00	0.00	0.00	0.00	0.01	0.00	0.00	0.00
Total	56.54	55.82	55.43	56.16	56.83	55.93	56.01	57.35	57.41	47.11	51.37	46.47	46.01
Structural formula based on 3 (O)													
Si	0.05	0.04	0.07	0.00	0.00	0.00	0.00	0.00	0.00	0.06	0.00	0.00	0.00
Ti	0.00	0.00	0.00	0.00	0.00	0.00	0.00	0.00	0.00	0.00	0.00	0.00	0.00
Al	0.00	0.00	0.00	0.00	0.00	0.00	0.00	0.00	0.00	0.00	0.00	0.00	0.00
Cr	0.00	0.00	0.00	0.00	0.00	0.00	0.00	0.00	0.00	0.00	0.00	0.00	0.00
Fe	0.03	0.03	0.04	0.01	0.01	0.02	0.01	0.01	0.01	0.03	0.31	0.10	0.09
Mn	0.05	0.07	0.10	0.00	0.00	0.00	0.00	0.00	0.00	0.06	0.01	0.01	0.02
Mg	0.21	0.24	0.20	0.07	0.10	0.03	0.04	0.10	0.11	2.78	2.67	2.88	2.88
Ca	2.59	2.58	2.53	2.92	2.89	2.95	2.95	2.89	2.87	0.01	0.01	0.01	0.01
Na	0.01	0.01	0.01	0.00	0.00	0.00	0.00	0.00	0.00	0.00	0.00	0.00	0.00
K	0.00	0.00	0.00	0.00	0.00	0.00	0.00	0.00	0.00	0.00	0.00	0.00	0.00
Ni	0.00	0.01	0.00	0.00	0.00	0.00	0.00	0.00	0.00	0.00	0.00	0.00	0.00
Total	2.95	2.97	2.94	3.00	3.00	3.00	3.00	3.00	3.00	2.94	3.00	3.00	3.00

TABLE IX. Continued

Rock type	Serpentinites									Pyroxenites			
Mineral	Magnesite									Dolomite			
Area	Madara									Kadaboura	Madara		
Sample No.	KK37b									KD217	KK37b	A	
Spot No.	#24	#39	#43	#56	#67	#103	#115	#126	#132	#9	#64	22	29
SiO_2	0.00	0.00	0.00	0.00	0.00	0.00	0.00	0.00	0.00	0.00	0.00	0.44	0.88
TiO_2	0.00	0.00	0.00	0.00	0.00	0.00	0.00	0.00	0.00	0.00	0.00	0.00	0.00
Al_2O_3	0.00	0.00	0.00	0.00	0.00	0.00	0.00	0.00	0.00	0.00	0.00	0.00	0.00
Cr_2O_3	0.00	0.00	0.00	0.00	0.00	0.00	0.00	0.00	0.00	0.00	0.00	0.00	0.00
FeO	3.40	10.00	9.10	10.12	3.86	11.15	3.38	3.34	3.00	0.13	0.17	0.23	0.24
MnO	0.05	0.10	0.32	0.04	0.06	0.13	0.22	0.22	0.10	0.00	0.05	0.00	0.05
MgO	44.45	41.05	41.92	41.44	45.32	39.92	44.02	44.34	44.15	20.90	21.03	20.18	18.79
CaO	0.13	0.22	0.27	0.12	0.15	0.24	0.20	0.22	0.20	31.65	31.25	35.03	33.48
Na_2O	0.00	0.00	0.00	0.00	0.00	0.00	0.00	0.00	0.00	0.00	0.00	0.10	0.06
K_2O	0.00	0.00	0.00	0.00	0.00	0.00	0.00	0.00	0.00	0.00	0.00	0.01	0.01
NiO	0.00	0.00	0.00	0.00	0.00	0.00	0.00	0.00	0.00	0.00	0.00	0.00	0.00
Total	48.02	51.38	51.61	51.72	49.38	51.43	47.82	48.12	47.45	52.68	52.50	55.98	53.55
Structural formula based on 3 (O)													
Si	0.00	0.00	0.00	0.00	0.00	0.00	0.00	0.00	0.00	0.00	0.00	0.02	0.04
Ti	0.00	0.00	0.00	0.00	0.00	0.00	0.00	0.00	0.00	0.00	0.00	0.00	0.00
Al	0.00	0.00	0.00	0.00	0.00	0.00	0.00	0.00	0.00	0.00	0.00	0.00	0.00
Cr	0.00	0.00	0.00	0.00	0.00	0.00	0.00	0.00	0.00	0.00	0.00	0.00	0.00
Fe	0.12	0.36	0.32	0.36	0.14	0.40	0.12	0.12	0.11	0.01	0.01	0.01	0.01
Mn	0.00	0.00	0.01	0.00	0.00	0.00	0.01	0.01	0.00	0.00	0.00	0.00	0.00
Mg	2.87	2.63	2.65	2.63	2.85	2.58	2.86	2.86	2.88	1.43	1.45	1.31	1.27
Ca	0.01	0.01	0.01	0.01	0.01	0.01	0.01	0.01	0.01	1.56	1.55	1.64	1.63
Na	0.00	0.00	0.00	0.00	0.00	0.00	0.00	0.00	0.00	0.00	0.00	0.01	0.01
K	0.00	0.00	0.00	0.00	0.00	0.00	0.00	0.00	0.00	0.00	0.00	0.00	0.00
Ni	0.00	0.00	0.00	0.00	0.00	0.00	0.00	0.00	0.00	0.00	0.00	0.00	0.00
Total	3.00	3.00	3.00	3.00	3.00	3.00	3.00	3.00	3.00	3.00	3.00	2.99	2.96